Systematic and Temporal Geochemical Changes in the Upper Deccan Lavas: Implications for the Magma Plumbing System of Flood Basalt Provinces

P. Hoyer, K. Haase, M. Regelous, Frédéric Fluteau

Geochemistry, Geophysics, Geosystems®

AGU ADVANCING EARTH AND SPACE SCIENCE

RESEARCH ARTICLE
10.1029/2022GC010750

Systematic and Temporal Geochemical Changes in the Upper Deccan Lavas: Implications for the Magma Plumbing System of Flood Basalt Provinces

P. A. Hoyer[1], K. M. Haase[1], M. Regelous[1], and F. Fluteau[2]

[1]Friedrich-Alexander-Universität Erlangen-Nürnberg, GeoZentrum Nordbayern, Erlangen, Germany, [2]Université Paris Cité, Institut de Physique du Globe de Paris, CNRS, Paris, France

Key Points:

- Four recharge-crystallization-eruption sequences fed the most voluminous Deccan lava
- Magmatic plumbing system with interconnected small- to medium-sized magma reservoirs
- Complex emplacement history including multiple stages of ascent, mixing, and storage

Supporting Information:

Supporting Information may be found in the online version of this article.

Correspondence to:

P. A. Hoyer,
patrick.hoyer@fau.de

Citation:

Hoyer, P. A., Haase, K. M., Regelous, M., & Fluteau, F. (2023). Systematic and temporal geochemical changes in the upper Deccan lavas: Implications for the magma plumbing system of flood basalt provinces. *Geochemistry, Geophysics, Geosystems*, *24*, e2022GC010750. https://doi.org/10.1029/2022GC010750

Received 19 OCT 2022
Accepted 26 JAN 2023

Author Contributions:

Conceptualization: P. A. Hoyer, K. M. Haase, M. Regelous
Funding acquisition: K. M. Haase
Investigation: P. A. Hoyer, M. Regelous
Resources: K. M. Haase, M. Regelous, F. Fluteau
Visualization: P. A. Hoyer
Writing – original draft: P. A. Hoyer, K. M. Haase, M. Regelous
Writing – review & editing: P. A. Hoyer, K. M. Haase, M. Regelous, F. Fluteau

Abstract Large Igneous Provinces (LIPs) are unusual volcanic events in which massive amounts of melt (~10^6 km^3) erupt in relatively short time periods (<10^6 years). Most LIP magmas have undergone extensive fractional crystallization and crustal contamination, but the crustal magmatic plumbing systems and the processes triggering eruptions are poorly understood. We present new major and trace element and radiogenic isotope data for 43 individual lava flows from a continuous 1,200 m thick stratigraphic profile through the upper, most voluminous part of the Deccan LIP (Bushe to Mahabaleshwar Formations). Eruption rates for this section are constrained by published paleomagnetic directions and absolute U-Pb ages for zircons from weathered flow tops exposed in the profile. We find four magmatic sequences each lasting ~10^4–~10^5 years during which major and trace element compositions change systematically, followed by an abrupt change in geochemistry at the start of a new sequence. Within each sequence, the MgO content and proportion of crustal contamination decrease progressively, indicating a continuous replenishment of the associated magma reservoirs with less contaminated but more evolved melts. These geochemical signatures are best explained by repeated episodes of melt recharge, mixing, and eruption of variably evolved magmas originating from relatively small magma reservoir located in different crustal levels.

Plain Language Summary Volcanism occurs predominantly at plate boundaries, either at mid-ocean ridges or subduction zones, where most mantle melts are produced. However, the Earth's history is punctuated by volcanic events which are not related to plate boundary processes and during which large amounts of melt erupt (~10^6 km^3) in relatively short periods of time (<10^6 years). These Large Igneous Provinces (LIPs) are associated with the activity of mantle plumes and eruption rates during their main stages are significantly higher than those of today's largest magmatic systems. However, since no LIP is currently active, the architecture of the associated plumbing systems is relatively unknown. In order to understand the magmatic processes during the emplacement of a LIP, we generated geochemical data from a continuous stratigraphic profile covering the most voluminous stage of the ~66 Ma Deccan LIP. By combining these new data with published paleomagnetic directions and absolute U-Pb ages for zircons, we found four eruption sequences each lasting ~10^4–~10^5 years. During these sequences, geochemical compositions change systematically, which is best explained by repeated episodes of melt recharge, mixing, and eruption of variably evolved magmas originating from relatively small magma reservoirs located at different crustal levels.

1. Introduction

Large Igneous Provinces (LIPs) represent the most extensive volcanic events on Earth during which massive amounts of melts (>10^6 km^3) erupt in relatively short periods of time (<1 Ma) (e.g., Bryan & Ernst, 2008). Many of these volcanic provinces were emplaced at the former positions of currently active hot spots and are thought to have formed due to extensive decompression melting of anomalously hot mantle triggered by an initiating mantle plume (Richards et al., 1989), usually accompanied by rifting (White & McKenzie, 1989) or delamination of the overlying continental lithosphere (Elkins-Tanton & Foulger, 2005). Single eruptive events probably consist of 10^3–10^4 km^3 of melt (e.g., Self et al., 2022), orders of magnitude greater than the volume of ~20 km^3 for the largest eruption on Iceland in the past 1,000 years (Self et al., 2014). Since no LIP is currently active, the structure of the associated magmatic plumbing systems and the processes triggering these voluminous eruptions are still debated (Ernst et al., 2005). It is generally accepted for active volcanic systems that primitive melt stagnate during their ascent at the crust-mantle boundary (Moho) as well as in middle or upper crustal levels, where they form

10.1029/2022GC010750

Figure 1. The schematic map of India showing the area of the Deccan Traps (dark gray) which consists of the Kachchh, Saurashtra, Malwa Plateau, Rajahmundry Traps, and Main Deccan Volcanic Province. The sub-provinces are separated from each other by the east-west trending Narmada Rift and north-south striking Cambay Rift. Profile X-X' marks a cross-section of the Main Deccan Volcanic Province, and the numbers represent the following Deccan formations: 1: Jawhar, 2: Igatpuri, 3: Thakurvadi, 4: Bhimashankar, 5: Khandala, 6: Bushe, 7: Poladpur, 8: Ambenali, and 9: Mahabaleshwar. The Jawhar to Bhimashankar Formations are the Kalsubai sub-group, the Khandala to Bushe Formations are the Lonavala sub-group, and the Poladpur to Mahabaleshwar Formations are the Wai sub-group. Figure modified from Schoene et al. (2019).

magma reservoirs (Cashman et al., 2017). Within these reservoirs, Fractional Crystallization (FC) leads to the precipitation of mafic mineral phases and volatile exsolution, changing the density, viscosity, and composition of the melts and enabling their ascent and eruption. However, the number of reservoirs in the magmatic plumbing system as well as their sizes and eruption frequencies are still unknown. Due to the enormous volumes of individual LIP flows, some models proposed that the associated magmatic plumbing systems consist of few large reservoirs with volumes between 10^5 and 10^6 km^3, whereby some are believed to be located at/or near Moho depth and the other within the upper continental crust (UCC) (Black & Manga, 2017; Karlstrom & Richards, 2011). Eruptions are assumed to be triggered by the interaction of these reservoirs, with primitive melts ascending from the lower ones into the upper ones, which results in pulsatory eruptions separated by volcanic hiatuses of ~10^5 years (Black & Manga, 2017; Karlstrom & Richards, 2011). In contrast, other studies propose that LIPs are fed by interconnected small- to medium-sized (10^2–10^3 km^3) magma reservoirs and individual eruptions are mainly caused by recharge-associated overpressure leading to more continuous volcanism with frequent eruptions (Mittal & Richards, 2021; Mittal et al., 2021).

The aim of our study is to test these two endmember models for LIP magma plumbing systems using major and trace element concentration as well as Sr-Nd-Pb isotope compositions of 43 lava flows sampled from a continuous ~1,200 m thick stratigraphic profile covering the most voluminous eruptions of the Deccan LIP, which were apparently erupted within about 10^5 years, and thus within the expected lifetime of the largest magma reservoirs. The use of geochemical data provides information about magmatic processes such as FC and magma mixing as well as assimilation of both lithospheric mantle and continental crust. Together with the thickness of the lava formations as well as absolute and relative time estimates between individual eruptions, it allows conclusions to be drawn about the sizes and eruptive mechanisms of the associated magma reservoirs.

2. Geological Background

The Deccan LIP covers ~0.5 × 10^6 km^2 of west central India (Jay & Widdowson, 2008; Mahoney, 1988), and the original extent is estimated at ~1.3 × 10^6 km^2 assuming large portions of the lavas have subsided beneath the Arabian Sea (Jay & Widdowson, 2008; Kumar & Chaubey, 2022) (Figure 1). The part of the Deccan LIP exposed on the Indian continent can be divided into four sub-provinces separated from each other by the east-west trending Narmada-Tapti Rift and the north-south striking Cambay Rift (Figure 1). The Kachchh and Saurashtra regions lie to the west of the latter, while the Malwa Plateau crops out to the east (Figure 1). The Main Deccan Volcanic Province is located south of the Narmada Rift (Figure 1). Since lavas from each of these regions have similar age and are connected via the age-progressive Chagos-Laccadive Ridge and the Mascarane Plateau to the active intraplate volcanoes of the island of Réunion, it is assumed that they were formed above the Réunion plume head during the break-up of India and the Seychelles microcontinent (e.g., Richards et al., 1989) The influence of a hot, deep mantle plume is moreover supported by time-reversed convection models (Glišović & Forte, 2017), elevated ^{3}He/^{4}He ratios measured in alkaline and picritic volcanic rocks sampled in the northern part of the Deccan LIP (e.g., Basu et al., 1993), and similarities in radiogenic isotope compositions of some Deccan lavas to basalts on Réunion (e.g., P. Lightfoot & Hawkesworth, 1988; Mahoney, 1988).

The Main Deccan Volcanic Province is the largest sub-province of the Deccan Traps and exposes a well-preserved stratigraphy with a combined thickness of ~3,500 m along the Western Ghats (Figure 1). Based on field observations as well as chemical and isotopic compositions, the lavas of the Main Deccan Volcanic Province were divided into three sub-groups and 12 formations, which are each several hundred meters thick (Beane et al., 1986;

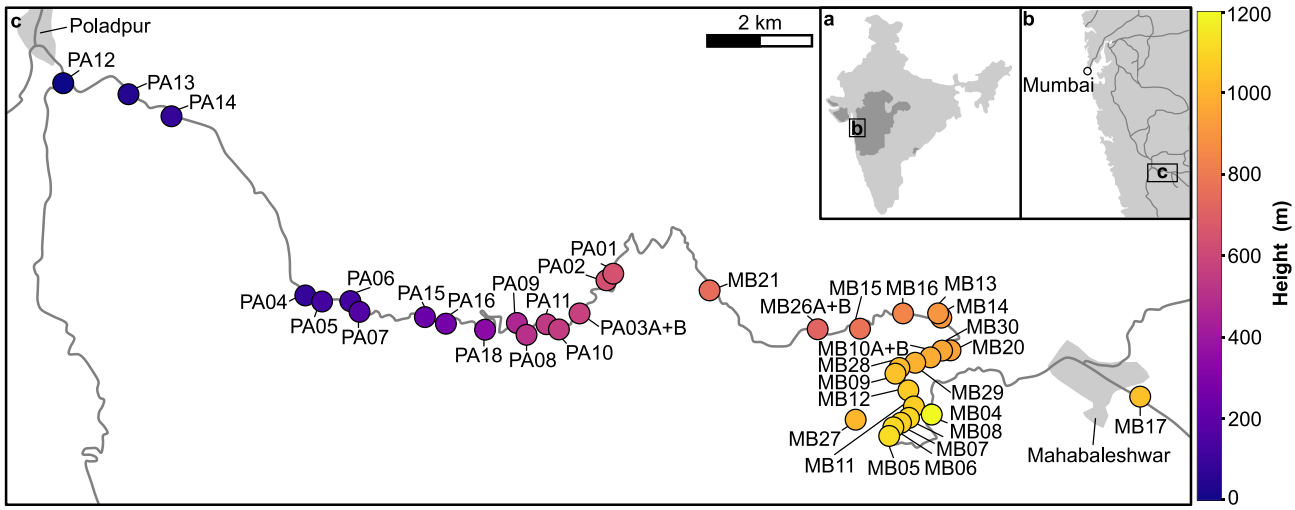

Figure 2. (a) Simplified map of the Indian peninsular showing the location of the Deccan Traps (dark gray). The black rectangle marks the sampling area given in panel (b). (b) Enlarged map of the Western Ghats region showing the exposed area of the Main Deccan volcanic Province. The black rectangle marks the sampling area shown in panel (c). (c) Detailed locations of samples taken along road outcrops between Poladpur and Mahabaleshwar. The colors of the sample points are coded according to their stratigraphic position. Figures are modified after Chenet et al. (2008).

K. G. Cox & Hawkesworth, 1985; P. C. Lightfoot et al., 1990) (Figure 1). Detailed field work revealed a regional north-south trending overstep sequence, indicating decreasing ages toward the southern Main Deccan Volcanic Province formations possibly due to the northward movement of the Indian Plate over the Réunion mantle plume (e.g., Devey & Lightfoot, 1986). The majority of the lavas of the Main Deccan Volcanic Province erupted during magnetochron C29r (Courtillot et al., 1986), and the most recent U-Pb and $^{40}Ar/^{39}Ar$ age dating indicates absolute ages between 66.4 and 65.4 Ma (Schoene et al., 2019; Sprain et al., 2019) overlapping in age with the biotic crisis at the Cretaceous-Paleogene boundary (KPB) (66.016 ± 0.050 Ma) (Schoene et al., 2019), in which ~75% of species became extinct (Sepkoski, 1996). However, because the age of the KPB coincides with the Chicxulub impact on Mexico, the relative roles of Deccan volcanism and impact in the end-Cretaceous mass extinction is debated (e.g., Alvarez et al., 1980; Punekar et al., 2014). Approximately 70% by volume of the total Deccan (Wai subgroup: Poladpur, Ambenali, and Mahabaleshwar formations) may have been erupted within the last 5×10^5 years of activity, beginning close to or several 10^4 years before the KPB (Schoene et al., 2019; Sprain et al., 2019). Studies using $^{40}Ar/^{39}Ar$ age dating place the KPB near to the base of the Poladpur Formation and suggest that the onset of the Wai eruptions began at the KPB potentially as a consequence of the Chicxulub impact (e.g., Sprain et al., 2019). In contrast, U-Pb zircon ages indicate that the Wai lavas were erupted in pulses, with the oldest Poladpur lavas erupted several 10^4 years before the KPB and the Ambenali lava in a second pulse ~10^5 years after the KPB (Schoene et al., 2019). Similar paleomagnetic directions for groups of adjacent Wai lava flows suggest that these may have been emplaced over timescales of less than a few hundred years (Chenet et al., 2008).

3. Material and Methods

3.1. Sampling of the Paleomagnetic Section

The samples analyzed in this work were previously collected and described by Chenet et al. (2008) for paleomagnetic studies. The authors drilled a total of 43 cores from fresh parts of well-exposed pahoehoe lobes from a ~1,200 m thick continuous section (hereafter referred as "MP section") covering the Bushe to Mahabaleshwar formations (K. Cox & Hawkesworth, 1984; K. G. Cox & Hawkesworth, 1985; Devey & Lightfoot, 1986; Jay, 2005) (Figure 2). The Bushe lavas exhibit nearly aphyric textures with abnormally coarse grain sizes compared to the overlying formations (Chenet et al., 2008). In contrast, the flows of the overlying Poladpur formation usually have a finer groundmass and display porphyritic textures with up to 15% phenocrysts of plagioclase ± clinopyroxene ± olivine (Chenet et al., 2008). The Ambenali formation consists of moderately to highly porphyritic rocks containing up to 25% phenocrysts of plagioclase ± clinopyroxene ± olivine (Chenet et al., 2008). In contrast,

the upper part of the formation is relatively phenocryst poor (Chenet et al., 2008). The Mahabaleshwar formation is built by well-defined lava flows showing increasing porphyritic textures with increasing height in the exposed sections (K. G. Cox & Hawkesworth, 1985; Jay, 2005). In the MP section, individual lava flows can be clearly distinguished from each other by the occurrence of chilled margins and reddish weathering horizons. The latter are believed to represent weathered flow tops indicating periods of volcanic quietness (Chenet et al., 2008; Duraiswami et al., 2020). Further details of the sampling strategy are given in Chenet et al. (2008).

3.2. Electron Microprobe Analyses

Following macroscopic observations, fresh and less altered samples were cut into small blocks and converted to polished thin sections. Based on microscopic characteristics, two samples (PA08 and PA10) were selected for mineral analysis and major and trace element compositions of plagioclase were carried out on a JEOL JXA-8200 Superprobe electron microprobe at the GeoZentrum Nordbayern, Friedrich-Alexander-Universität Erlangen-Nürnberg. The microprobe operated with an acceleration voltage of 15 kV, a beam current of 15 nA and a focused beam. Counting times were set to 20 and 10 s for peaks and backgrounds. The major element data are shown in Table S1 in Supporting Information S1.

3.3. Whole Rock Major and Trace Element Analyses

A total of 43 drill cores were cut into blocks with a rock saw for geochemical analyses. Thereafter, the pieces were cleaned in an ultrasonic bath with deionized water and dried at 60°C for 12 hr. Subsequently, the blocks were coarsely crushed using a hydraulic press and pulverized in an agate mill. Prior further geochemical analyses, the powders were dried at 105°C for 12 hr. For major and selected trace element measurements, whole-rock powders were mixed with lithium tetraborate, fused to glass beads and analyzed using a Spectro XEPOS He X-ray fluorescence spectrometer at the GeoZentrum Nordbayern, Friedrich-Alexander-Universität Erlangen-Nürnberg. Repeated measurements ($n = 9$) of the international rock standard BE-N yielded a precision better than 1.3%, and an accuracy better than 3.1%, except for P_2O_5 (13.1%). Trace element analyses were carried out by solution ICP-MS at Erlangen. Multiple analyses of the BHVO-2 Hawaiian rock standard give accuracy and precision better than 5% and 3%, respectively. Details about the analytical procedure are presented in Hoyer, Haase, et al. (2022). The major and trace element data are shown in Table S2. Note that the trace element concentrations for Zr, Nb, Ba, La, Sm, Dy, Yb, and Th were previously published by Hoyer, Regelous, et al. (2022).

3.4. Whole Rock Radiogenic Isotope Analyses

For radiogenic isotope analyzes, approximately 150 mg of sample powder was dissolved in 15 drops double distilled 15M HNO_3 and 25 drops double distilled 12M HF in sealed Teflon Beakers at 80°C overnight. Subsequently, the samples were evaporated at 120°C to near dryness and redissolved in 20 drops double distilled 15M HNO_3. After the samples have been completely steamed off, they were redissolved in 30 drops double distilled 6M HCl and evaporated again. Then, the samples were finally dissolved in 30 drops double distilled 1M HCl. To separate the solution from the undissolved residual solid material, the samples were transferred in 2 ml microtubes and centrifuged for 5 min at 5,000 rpm. Subsequently, the severed sample solution was loaded onto 100 µl Eichrom Sr-Spec resin. Afterward, 4 × 15 drops double distilled 1M HCl was added to wash out the Sr and REE fractions before collecting Pb in 4 × 20 drops double distilled 6M HCl. Then, the Pb solution was evaporated, redissolved in 10 drops double distilled 1M HCl and loaded again on the Sr-Spec. Once the sample solution passed the columns, 4 × 15 drops double distilled 1M HCl was added before finally Pb was collected in 4 × 20 drops double distilled 6M HCl. After drying the Pb solution it was redissolved in 2% HNO_3. The retained Sr and REE fractions were mixed with the undissolved solid material from the Pb collection and evaporated to dryness at 120°C. Then, the mixtures were redissolved in 2 ml 1M HCl + 0.1 M HF in sealed Teflon Beakers at 70°C overnight. Subsequently, the solutions were transferred in plastic tubes and centrifuged for 5 min at 5,000 rpm. Thereafter, the separated liquid parts have been loaded on columns filled with 100 µl Eichrom Sr-Spec resin and 150 µl Eichrom TRU-Spec resin. When the sample solutions have passed through the resins, the latter were rinsed with 6 ml 1M HCl + 0.1 M HF and 26 ml 2.5 M HCl. Subsequently, Sr was collected in 12 ml 2.5 M HCl. Then, 10 ml 2.5 M HCL and 4 ml 6M HCl were added before collecting Nd and Sm in 10 ml 6M HCl. The gathered Sr fractions were evaporated to dryness and redissolved in 3.5 M HNO_3. Then, the solutions were loaded

on the same Sr-Spec resins which were used for Pb separation. After Ca was washed out by adding 2 × 3.5 M HNO_3, Sr was re-collected in MQ H_2O. Subsequently, the Sr-solution was fumed off, redissolved in 1M H_3PO_4 and loaded onto Ta single filaments. For Nd separation, the Nd-Sm fractions were evaporated, redissolved in 0.5 ml 0.25 M HCl and loaded on columns filled with 1.5 ml Eichrom LN-Spec resin. After rinsed with 6.5 ml 0.25 M HCl, Nd was collected in 12 ml 0.25 M HCl. The latter were evaporated, redissolved in 0.1 H_3PO_4 and loaded on Ta filaments facing Re filaments. Lead isotope measurements were carried out on a Thermo Scientific Neptune Plus High Resolution Multicollector ICP-MS (MC-ICP-MS) at the GeoZentrum Nordbayern in Erlangen, Germany. To correct instrumental mass fractionation, a $^{207}Pb/^{204}Pb$ (ratio = 0.85) double spike calibrated against the NBS981 lead isotope standard has been used. The samples dissolved in 2% HNO_3 were diluted to a concentration of ~20 ppb, whereby an aliquot of this solution was spiked to obtain a $^{208}Pb/^{204}Pb$ ratio of about 1. Both sample solutions were fed into the plasma via a Cetac Aridus desolvating nebulizer. Repeated measurements of the NBS981 lead isotope standard gave average $^{206}Pb/^{204}Pb$, $^{207}Pb/^{204}Pb$, and $^{208}Pb/^{204}Pb$ ratios of 16.9420 ± 0.0016, 15.4994 ± 0.0016, and 36.7239 ± 0.0043 (n = 21) and are normalized to values of 16.9410, 15.4993, 36.7233 for NBS981. Sr and Nd isotope measurements were determined in a static mode on a Thermo Scientific Triton Series Multicollector Thermal Ionization Mass Spectrometer at the GeoZentrum Nordbayern in Erlangen, Germany. Corrections for instrumental mass fractionation were made by using a $^{88}Sr/^{86}Sr$ ratio of 0.1194. Neodymium isotopic data were corrected for mass fractionation by assuming $^{146}Nd/1^{44}Nd = 0.7219$. Repeated measurements of the NBS987 Sr isotope standard gave average $^{87}Sr/^{86}Sr$ ratios of 0.710265 ± 0.000012 (n = 12) and are normalized to a value of 0.710250 for NBS987, while the "Erlangen Nd" standard solution yielded average $^{143}Nd/^{144}Nd$ ratios of 0.511541 ± 0.000008 (n = 8), which is equivalent to a value of 0.511850 for the La Jolla Nd isotope standard. All isotope ratios were age-corrected for an assumed age of 66 Ma. The Sr-Nd-Pb isotope data are shown in Table S2.

4. Results

4.1. Petrography and Mineral Compositions

The majority of lavas of the MP section show a glomeroporphyritic texture consisting of aggregated phenocrysts of plagioclase, clinopyroxene and olivine embedded in a fine-grained matrix of plagioclase and clinopyroxene. Plagioclase phenocrysts are 3–5 mm long and exhibit a hypidiomorphic, tabular form. Most crystals show lamellar twinning, while some are zoned and/or exhibit sieve textures. The plagioclase phenocrysts are randomly orientated, but often form clusters with clinopyroxene. Electron microprobe backscatter electron images show that plagioclase exhibits compositional zoning (Figure 3). The phenocrysts commonly have overgrowth rims which are more sodic (anorthite content: 0.54–0.66) than the cores (anorthite content: 0.70–0.80) (Figure 3). The boundaries between core and rim overgrowth are sharp and characterized by a compositional gap rather than a gradual decrease in anorthite content (Figure 3). The clinopyroxene phenocrysts are 2–3 mm across, have a hypidiomorphic form, and some exhibit sieve textures. Olivine is subordinate and only a few small (1–2 mm sized) crystals are clearly identifiable.

4.2. Stratigraphic Variations in Lava Geochemistry

Between the base of the profile and ~200, ~200 and ~680, ~680 and ~970 m as well as ~970 and ~1,200 m height, the lavas of the MP section show four repeating sequences (hereafter referred as S1 to S4) of upwards increasing or decreasing major element characteristics (Figure 4). Each of these sequences is initiated by a sudden increase in MgO and Al_2O_3 as well as a decrease in TiO_2 and FeO^T (Figure 4). Subsequently, MgO and Al_2O_3 gradually decrease, while TiO_2 and FeO^T continuously increase until a rapid shift of these major element oxides to higher or lower values marks the beginning of a new sequence (Figure 4).

Nb/Th and Ce/Pb show similar geochemical patterns as described above, whereby the earliest lavas in each sequence have low ratios, which progressively increase with height (Figures 5a and 5b). Compared to the major element oxides, the transitions between the different sequences are more gradually rather than sharp (Figures 5a and 5b). Between the lowermost lava flow and ~370 m height, La/Sm shows similar geochemical trends as Nb/Th and Ce/Pb (Figures 5a–5c). Above ~370 m height, La/Sm variations are minor, with the ratio gradually decreasing above ~930 until ~1,030 m, where it reverses and then increases again (Figure 5c). Compared to the other trace element ratios, those of Nb/Zr increase continuously between the lowermost lava flow and ~930 m height

10.1029/2022GC010750

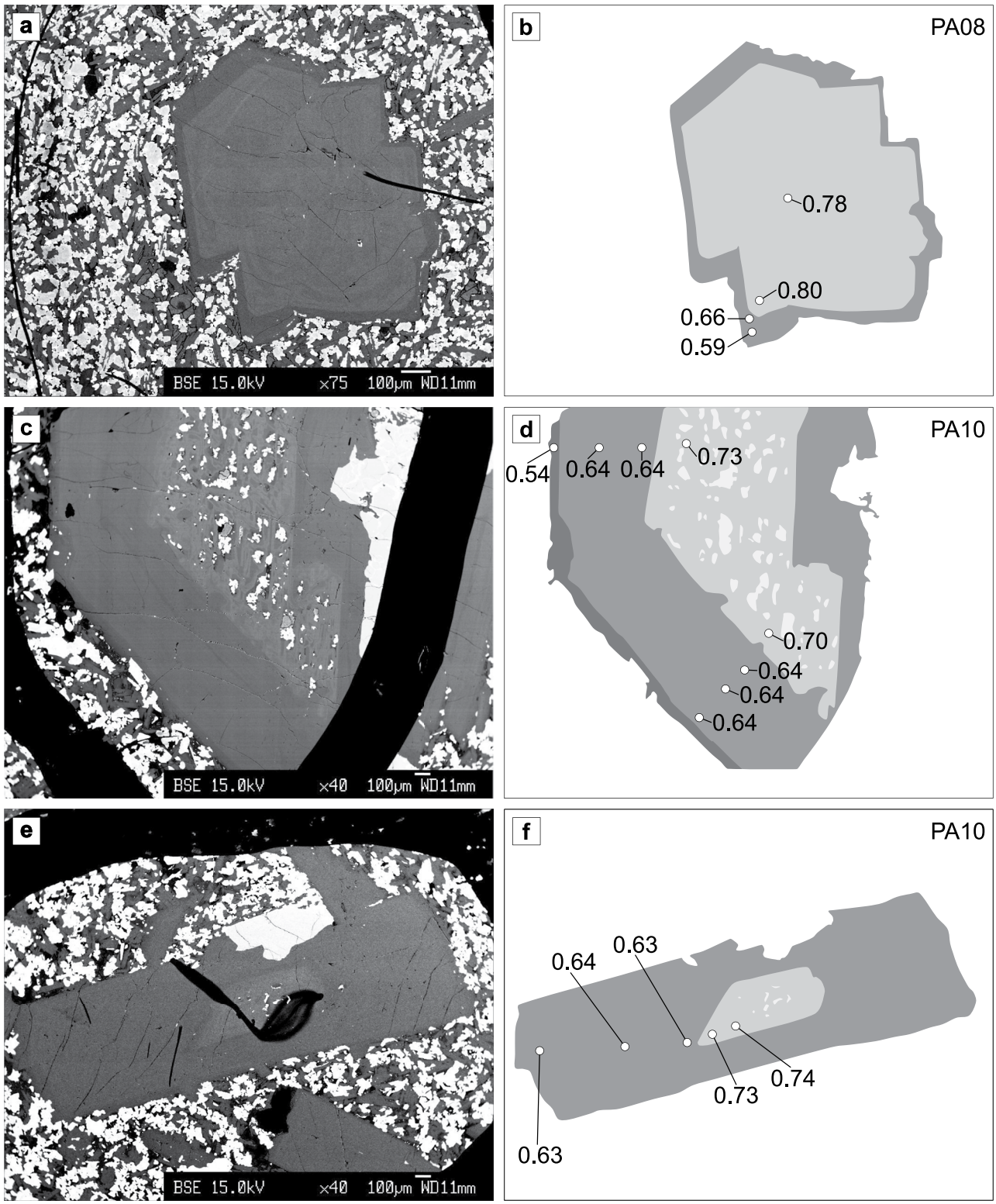

Figure 3.

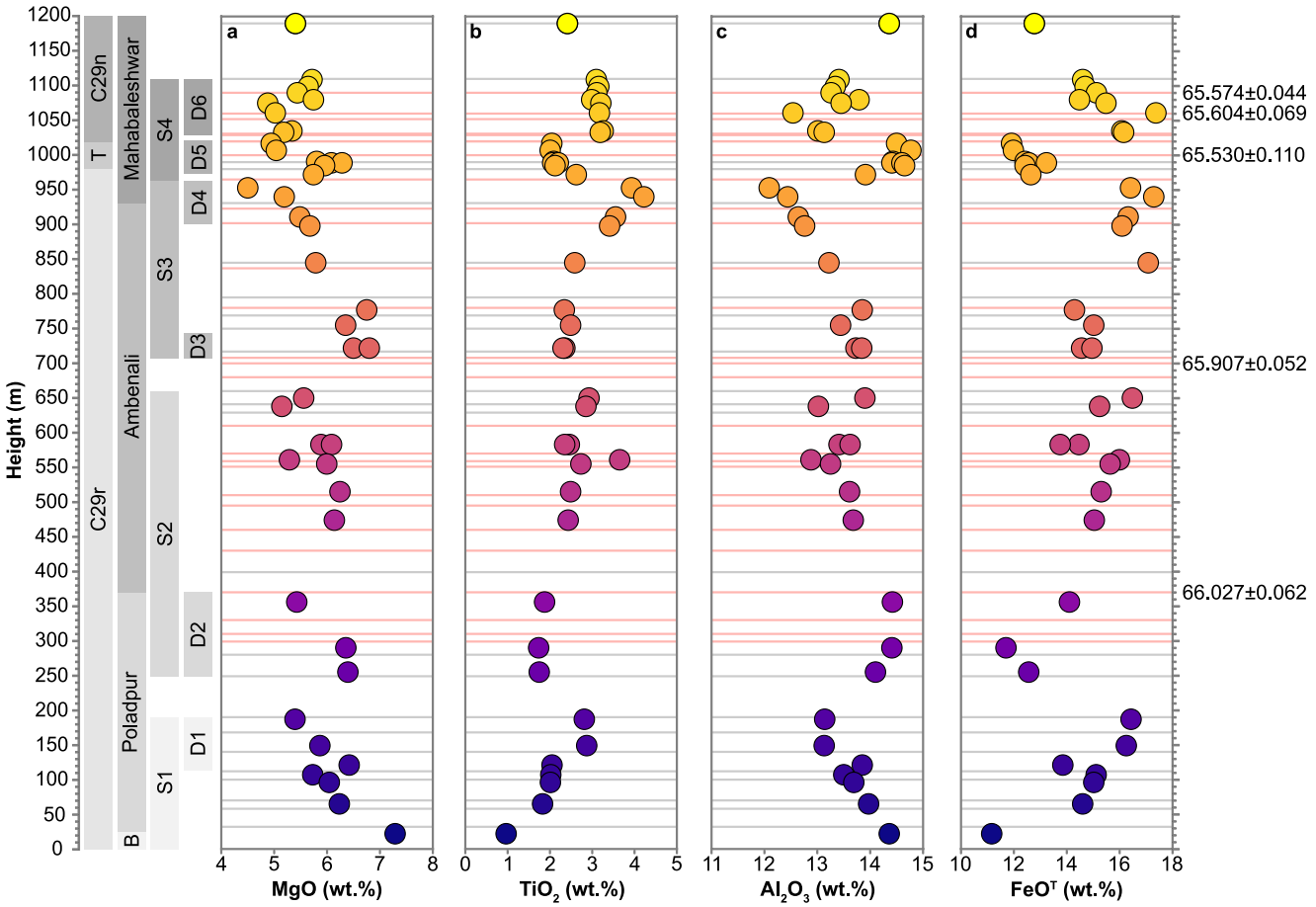

Figure 4. Major element variation in lavas with stratigraphic height. (a) MgO, (b) TiO_2, (c) Al_2O_3, (d) FeO^T. The boundaries between Bushe and Poladpur, Poladpur and Ambenali, and Ambenali and Mahabaleshwar lie between 25, 370, and 934 m, respectively. Between 0 and 980 m stratigraphic height, the lava samples exhibit normal polarity, while between 980 and 1,020 m and between 1,020 and 1,200 m they show transitional and reversed polarity, respectively (Chenet et al., 2008). Light gray lines are chilled margins and light red lines are red boles representing weathered flow tops; both indicate boundaries between individual lava flows. Zircons separated from five red boles from this section yielded absolute U-Pb ages which are given in million years (Schoene et al., 2019). The lavas of the MP profile were emplaced in four sequences (S1 to S4). S1 lies between the base of the profile and ~200 m height, S2 lies between ~200 and ~680 m height, S3 lies between ~700 and ~970 m height, and S4 lies between ~980 and ~1,100 m height. Note that the samples were previously analyzed for paleomagnetic directions (Chenet et al., 2008). It is assumed that lava flows that statistically have the same paleomagnetic directions (range of 5°–10°) have been formed within very short periods of time (~4×10^2 years) and form so-called Directional Groups (DGs), which indicate almost simultaneous emplacement (Chenet et al., 2008). Note that the DGs are located either at the bottom or top of a sequence with DG 1 is located at the top of S1, DG2 is located at the base of the S2, DG3 and DG 4 are located at the base respectively top of S3 and DG 5 and DG 6 are located at the bottom respectively top of S4. Abbreviations are as follows: S1 to S4: sequences 1 to 4; D1 to D6: Directional Groups 1 to 6; T: Transitional polarity; and B: Bushe.

without significant geochemical variations (Figure 5d). At ~930 m height, Nb/Zr shows a sharp break toward significantly higher ratios and then progressively decreases again with increasing height (Figure 5d).

Initial $^{87}Sr/^{86}Sr$ ratios generally decrease with height, but three samples have higher values (at ~22, ~255, and ~845 m height, Figure 6a). εNd_{66Ma} values slightly increase upsection toward ~930 m with two negative outliers at ~22 and ~255 m height (these samples also have higher $^{87}Sr/^{86}Sr$). From ~930 m, ratios of εNd_{66Ma}

Figure 3. Electron microprobe backscatter electron images of plagioclase phenocrysts. The plagioclases exhibited compositional zoning, whereby the Ca-rich cores were overgrown by more sodic rims. The boundaries between core and rim overgrowth are sharp and characterized by a compositional gap rather than a gradual decrease in anorthite content (An = Ca/[Ca + Na]). (a) Plagioclase phenocryst with sodic overgrowth rim. (b) Schematic drawing of plagioclase phenocryst given in panel (a). The core displays contents between ~0.78 and ~0.80, while the rim exhibits contents between ~0.59 and ~0.66. (c) Plagioclase phenocryst with multiple sodic overgrowth rims. The core is resorbed and exhibits sieve textures. (d) Schematic drawing of plagioclase phenocryst given in panel (c). The core displays contents between ~0.70 and ~0.73, the first rim exhibits an contents of ~0.63 and the second rim have an contents of ~0.54, respectively. (e) Plagioclase phenocryst with resorbed Ca-rich core and more sodic overgrowth rim. (f) Schematic drawing of plagioclase phenocryst given in panel (e). The core displays contents between ~0.73 and ~0.74, while the rim exhibits contents between ~0.63 and ~0.64.

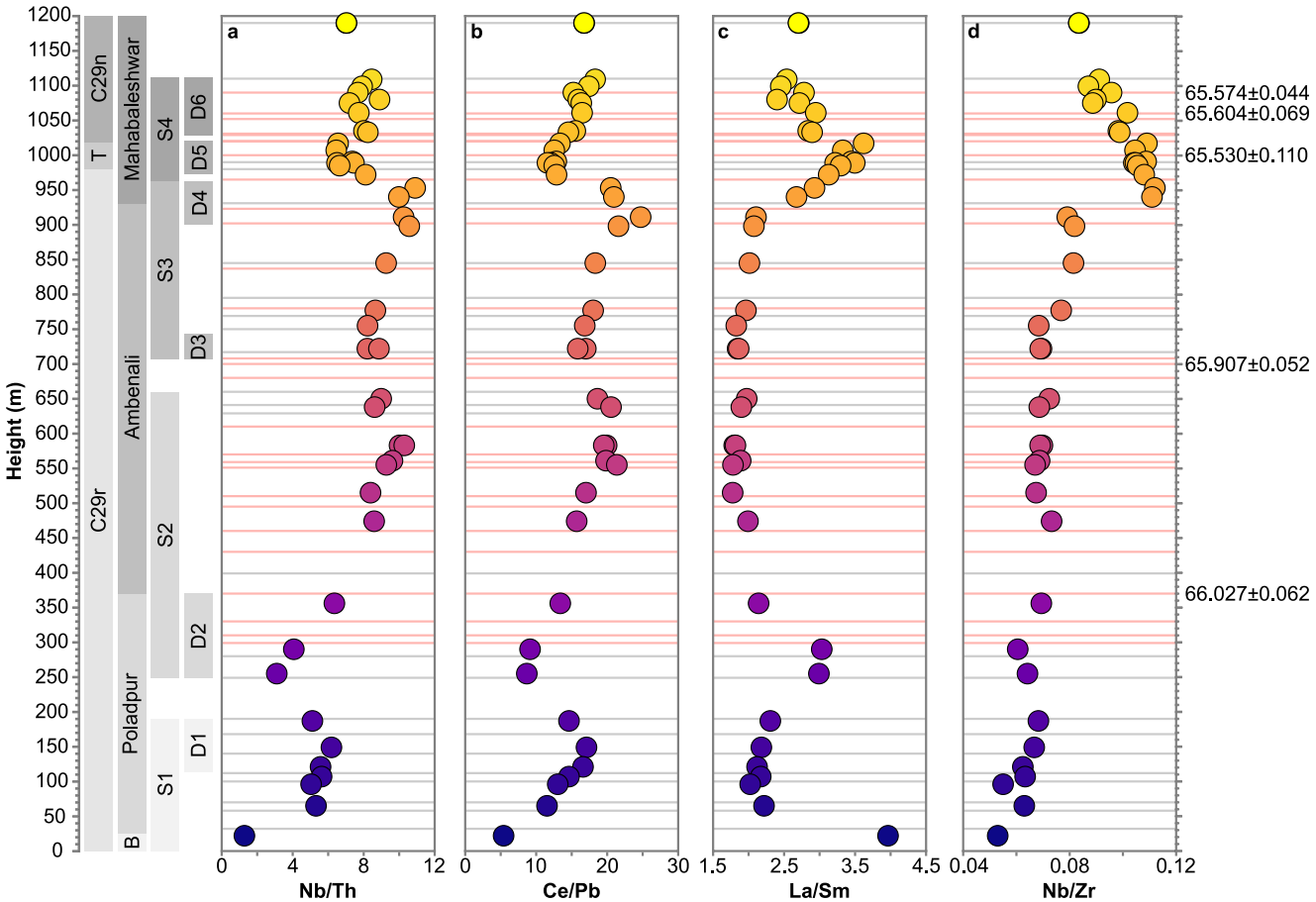

Figure 5. Variations in trace element ratios with stratigraphic height. (a) Nb/Th, (b) Ce/Pb, (c) La/Sm, and (d) Nb/Zr. Variations in Nb/Th and Ce/Pb reflect different degrees of crustal contamination, with high ratios indicating low degrees and low ratios indicating high degrees, respectively. Within each sequence, the amount of crustal contamination progressively decreases with height. With the transition to the Mahabaleshwar Formation, the ratios of La/Sm and Nb/Zr rapidly shift toward higher values, possibly indicating a change in the composition and depth of the contamination end-member. Abbreviations are as follows: S1 to S4: sequences 1 to 4; D1 to D6: Directional Groups 1 to 6; T: Transitional polarity; and B: Bushe.

progressively decrease until ~1,000 m, where it reverses and increases again (Figure 6b). In comparison, between the lowermost lava flow and a red bole located at ~970 m height, the ratios of $^{206}Pb/^{204}Pb_{66Ma}$ and $^{208}Pb/^{204}Pb_{66Ma}$ gradually decreased (Figures 6c and 6d). The lava directly above show a rapid shift toward lower ratios, but then gradually increase and again follow the general decreasing trend of the profile (Figures 6c and 6d).

4.3. Correlated Variations Between Major and Trace Element and Isotope Compositions

The lavas of the MP section display a rough negative correlation between MgO and TiO_2 and a positive correlation between MgO and Al_2O_3 (Figures 7a and 7b). However, the samples do not show a continuous geochemical evolution with time, which would be indicated by a systematic increase or decrease in the MgO content with stratigraphic height (Figures 7a and 7b). Instead, the MgO contents of the Bushe to Poladpur lavas (7.3–5.4 wt.%) overlap with those of the Ambenali (6.8–5.2 wt.%) and Mahabaleshwar formations (7.1–4.5 wt.%) (Figures 7a and 7b). The lava comprising the lower third of the MP section (up to ~400 m height) show a negative correlation between MgO and Nb/Th and Ce/Pb (Figures 7c and 7d). Along this general trend, the MgO content varies between 5.4 and 7.3 wt.%, with the lava with the highest MgO contents having the lowest Nb/Th and Ce/Pb contents, respectively (Figures 7c and 7d). In comparison, the overlying lava (~400–~1,200 m height) display variable Nb/Th and Ce/Pb at given MgO without showing clear geochemical trend (Figures 7c and 7d).

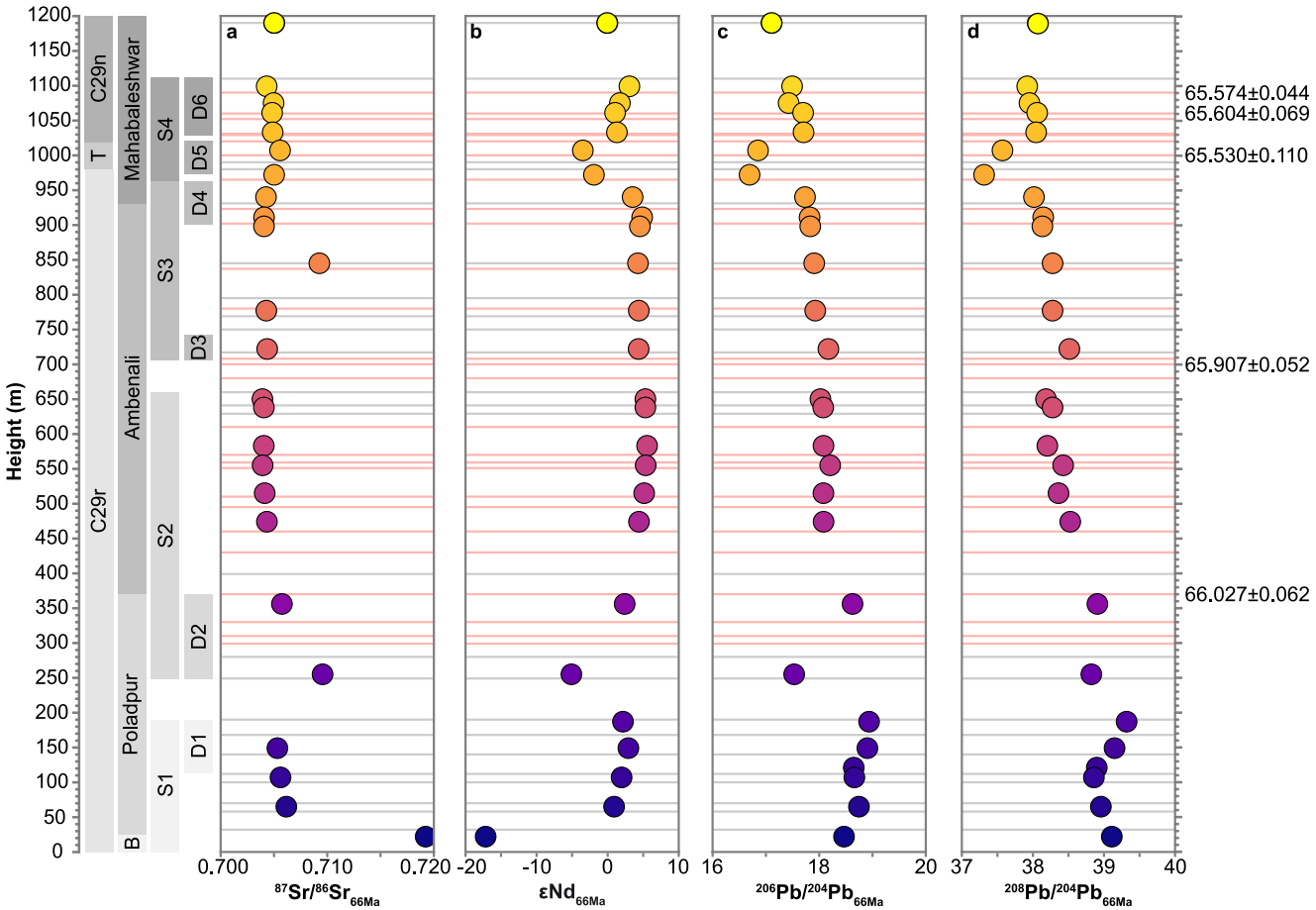

Figure 6. Variations in radiogenic isotope ratios with stratigraphic height. (a) $^{87}Sr/^{86}Sr_{66Ma}$, (b) εNd_{66Ma}, (c) $^{206}Pb/^{204}Pb_{66Ma}$, and (d) $^{208}Pb/^{204}Pb_{66Ma}$. $^{87}Sr/^{86}Sr_{66Ma}$, $^{206}Pb/^{204}Pb_{66Ma}$, and $^{208}Pb/^{204}Pb_{66Ma}$ gradually decrease with height, while εNd_{66Ma} progressively increase with height. Outliers are at ~22 ($^{87}Sr/^{86}Sr_{66Ma}$, εNd_{66Ma}), ~255 ($^{87}Sr/^{86}Sr$, εNd_{66Ma}, $^{206}Pb/^{204}Pb_{66Ma}$), and ~845 m ($^{87}Sr/^{86}Sr_{66Ma}$, εNd_{66Ma}) height. With the transition to the Mahabaleshwar Formation, ratios of εNd_{66Ma}, $^{206}Pb/^{204}Pb_{66Ma}$, and $^{208}Pb/^{204}Pb_{66Ma}$ rapidly shift toward lower values possibly indicating a change in the composition and depth of the contamination end-member. Abbreviations are as follows: S1 to S4: sequences 1 to 4; D1 to D6: Directional Groups 1 to 6; T: Transitional polarity; and B: Bushe.

The Ambenali lavas show high εNd_{66Ma} (~3.5–~5.6), moderate $^{206}Pb/^{204}Pb$ (17.7–18.2) and $^{208}Pb/^{204}Pb$ (38.0–38.5) as well as low $^{87}Sr/^{86}Sr$ (~0.704, one sample with 0.709) and Nb/Zr (~0.06–~0.07) and plot on an array between Réunion Island basalts and Indian Mid-Ocean Ridge Basalt (MORB) (Figure 8). In comparison, the Poladpur and Bushe lavas exhibit higher $^{87}Sr/^{86}Sr$ (0.705–0.719), $^{206}Pb/^{204}Pb$ (17.5–18.9), $^{208}Pb/^{204}Pb$ (38.8–39.3) as well as lower εNd_{66Ma} (−17.2 to 2.9) and Nb/Zr (~0.05–~0.06) and lie between those of the Ambenali formation and felsic rocks of the UCC as well as mafic granulites and amphibolites (Figure 8). The Mahabaleshwar lavas display low $^{87}Sr/^{86}Sr$ (0.704–0.706), $^{206}Pb/^{204}Pb$ (16.9–17.7), $^{208}Pb/^{204}Pb$ (37.3–38.1), and εNd_{66Ma} (−3.5 to 3.0) as well as high Nb/Zr (~0.07–~0.12), and plot on an array between the Ambenali formation and an endmember with low $^{87}Sr/^{86}Sr$, $^{206}Pb/^{204}Pb$, $^{208}Pb/^{204}Pb$, and εNd_{66Ma} but high Nb/Zr (Figure 8). In general, published data from the Wai Formations (Basu et al., 2020) follow these geochemical trends, with some lavas of the Mahabaleshwar Formation showing significantly higher Nb/Zr (~0.15–~0.17) and partly overlapping with the basalts of the Reunion Islands (Figure 8).

5. Discussion

5.1. Refining the Stratigraphy of the MP Section

Based on volcanic rocks obtained from the MP section, previous petrological and geochemical studies defined the boundaries between the Bushe, Poladpur, Ambenali, and Mahabaleshwar formations (K. Cox & Hawkesworth, 1984;

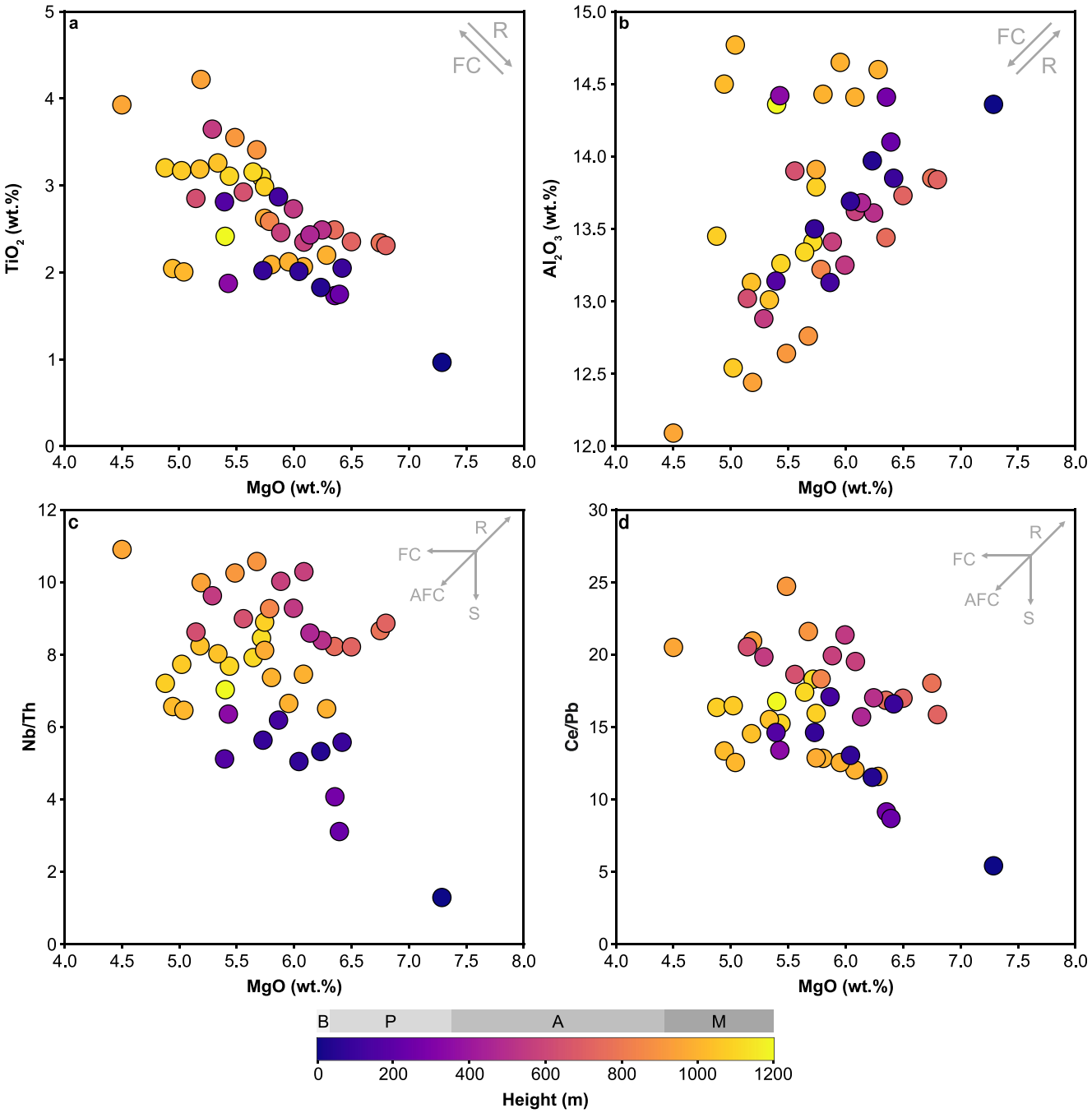

Figure 7. Bivariation plots between (a) MgO and TiO_2, (b) MgO and Al_2O_3, (c) MgO and Nb/Th, and (d) MgO and Ce/Pb. (a, b) No continuous geochemical evolution with stratigraphic height. The MgO contents of the Bushe to Poladpur lavas (7.3–5.4 wt.%) overlap with those of the Ambenali (6.8–5.2 wt.%), and Mahabaleshwar Formations (7.1–4.5 wt.%) indicating multiple fractional crystallization (FC) trends which are unlikely to be associated with a single large magma reservoir. (c, d) No evidence for continuous assimilation-fractional-crystallization (AFC) processes. If AFC processes had been important during the genesis of the Wai basalts, they should exhibit a positive correlation between MgO (parameter of fractionation) and Nb/Th as well as Ce/Pb (portion of crustal material), indicating increasing contamination with increasing FC. In contrast, the least fractionated lavas generally have the lowest Ce/Pb and Nb/Th. The colors of the data points are coded according to their stratigraphic position. Abbreviations are as follows: AFC: Assimilation-Fractional-Crystallization; FC: Fractional Crystallization; S: Source Heterogeneity; R: Melt Recharge; B: Bushe; P: Polapdur; A: Ambenali; and M: Mahabaleshwar.

K. G. Cox & Hawkesworth, 1985; Devey & Lightfoot, 1986; Najafi et al., 1981). The geochemical stratigraphy is based on the one hand on variations in TiO_2, Y, Zr, Nb, and Mg# used as monitors of FC and on the other hand on Ba, Rb, K_2O, SiO_2, and $^{87}Sr/^{86}Sr$ as sensitive proxies of crustal contamination (e.g., K. G. Cox & Hawkesworth, 1985). It is debated whether the lowermost part of the lava stack belongs to the Bushe (Devey

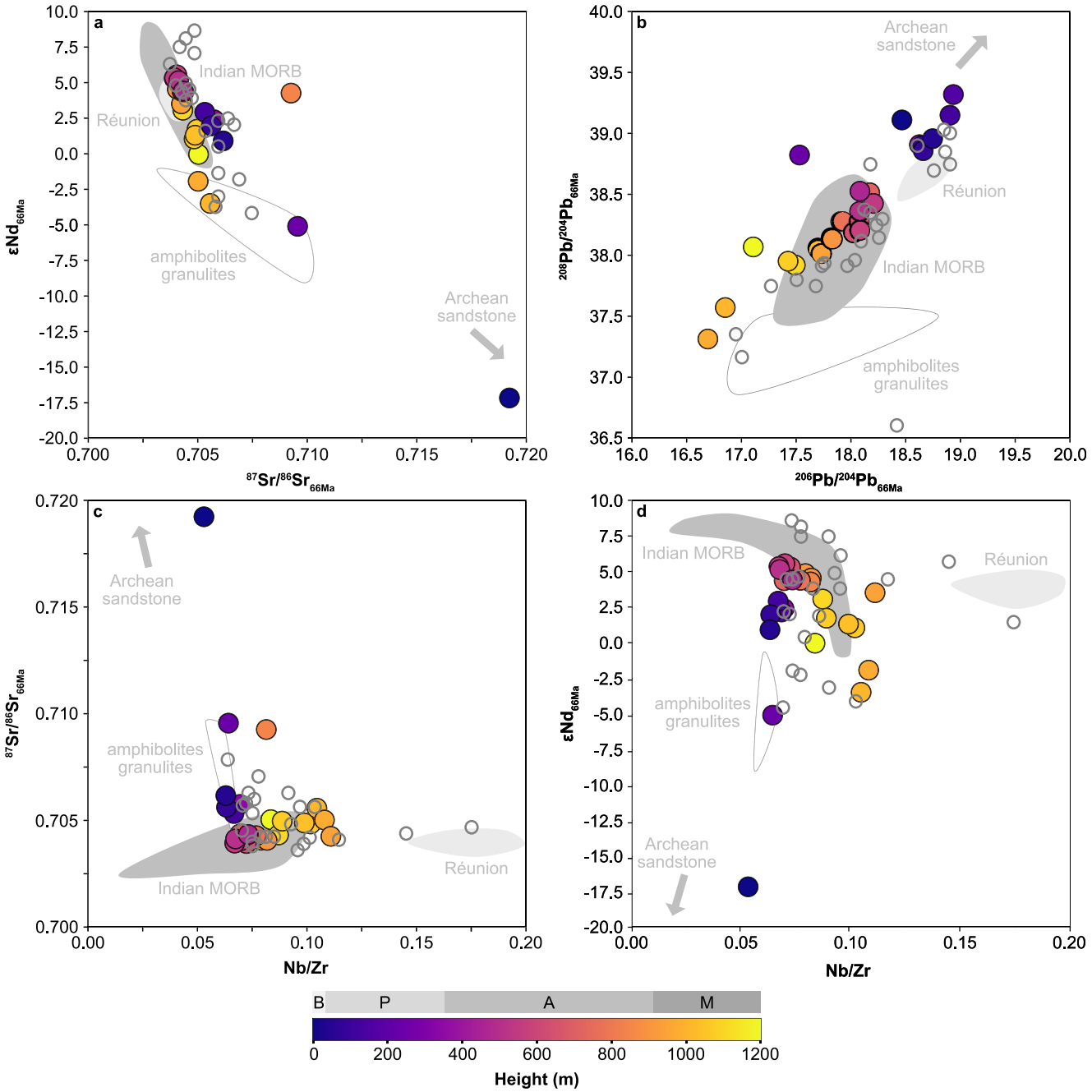

Figure 8. Bivariation plots between (a) $^{87}Sr/^{86}Sr_{66Ma}$ and εNd_{66Ma}, (b) $^{206}Pb/^{204}Pb_{66Ma}$ and $^{208}Pb/^{204}Pb_{66Ma}$, (c) Nb/Zr and εNd_{66Ma}, and (d) Nb/Zr and $^{87}Sr/^{86}Sr_{66Ma}$ showing multiple assimilation trends for the Bushe to Mahabaleshwar lavas. The Ambenali lavas are assumed to be relatively uncontaminated, reflecting the mixing of enriched Reunion-type and depleted Indian Mid-Ocean Ridge Basalt (MORB)-type mantle. The Bushe and Poladpur lavas possibly reflect mixing between Ambenali-type lavas and both lower (mafic granulites and amphibolites) and an upper crustal component (Archean sandstone), which could indicate multiple periods of storage and assimilation during melt ascent. The Mahabaleshwar lavas exhibit different Sr-Nd-Pb isotope compositions, in particular lower $^{206}Pb/^{204}Pb$ ratios similar to lower crustal components (mafic granulites and amphibolites). Published data from the Wai Formation (open circles, Basu et al., 2020) follows these geochemical trends, with some lavas of the Mabahaleshwar Formation showing significantly higher Nb/Zr. Abbreviations are as follows: MORB: Mid-Ocean Ridge Basalt; B: Bushe; P: Polapdur; A: Ambenali; M: Mahabaleshwar. Indian MORB data sources: Chauvel and Blichert-Toft (2001) and references therein. Réunion data sources: Albarede et al. (1997), Bosch et al. (2008), and Luais (2004). Lower crustal component (amphibolite and granulite) data sources: Wang et al. (2013).

& Lightfoot, 1986; Jay, 2005) or Poladpur formation (e.g., Chenet et al., 2008; K. Cox & Hawkesworth, 1984). The Bushe formation is characterized by relatively high $^{87}Sr/^{86}Sr$ (0.713–0.720) and SiO_2 (>50 wt.%) as well as low εNd (−13 to −18) and TiO_2 (<2 wt.%) and possibly represents lava which were highly contaminated with an Archean granitic crustal endmember (e.g., Beane et al., 1986; K. G. Cox & Hawkesworth, 1985; P. Lightfoot &

Hawkesworth, 1988). Our lowermost lava sample located at ~22 m stratigraphic height (PA 12) exhibits these geochemical characteristics and can accordingly be assigned to the Bushe formation (Figures 4 and 6). In contrast, the next sample above at ~65 m (PA 13) displays much lower $^{87}Sr/^{86}Sr$ (0.706) and εNd_{66Ma} (0.9) and therefore belongs to the Poladpur formation (Figure 6). Thus, the Bushe—Poladpur boundary must be located in the section between. Unfortunately, most of the lavas of the lowermost part of the MP section are highly weathered and/or poorly exposed (Chenet et al., 2008; Jay, 2005). Consistent with this, recent field observations found evidence for a disconformity at the Bushe-Poladpur contact, possibly indicating a period of volcanic quietness and extensive weathering (Richards et al., 2015). For this reason, we set the boundary between these formations within the MP section at 25 m stratigraphic height which can be considered as a lower limit.

The boundary between the Poladpur and Ambenali formations was previously associated with a red bole located at ~370 m stratigraphic height (Chenet et al., 2008) (Figures 4–6). Recent U-Pb geochronology on separated zircons from this weathered horizon yielded an absolute age of 66.027 ± 0.062 Ma (Schoene et al., 2019). The Poladpur formation is believed to be contaminated to intermediate degrees with the same endmember as the Bushe formation, whereas the overlying Ambenali lavas are assumed to be the least contaminated of the entire Main Deccan Volcanic Province (P. Lightfoot & Hawkesworth, 1988; Mahoney, 1988). The lavas between ~25 and ~370 m stratigraphic height exhibit highly variable ratios of $^{206}Pb/^{204}Pb_{66Ma}$, $^{208}Pb/^{204}Pb_{66Ma}$, $^{87}Sr/^{86}Sr_{66Ma}$, and εNd_{66Ma} as well as of Nb/Th and Ce/Pb indicating considerable assimilation of a Bushe-type endmember (Figures 5, 6, and 8). In contrast, the lava above ~370 m height are comparatively homogenous, showing no clear evidence of extensive contamination (Figures 5, 6, and 8). For this reason, we can confirm the previously defined location of the Poladpur—Ambenali boundary at 370 m.

The boundary between the Ambenali and Mahabaleshwar formations was previously set at ~934 m stratigraphic height and is mainly based on a rapid increase in the ratios of $^{87}Sr/^{86}Sr$ and Ba/Y (K. G. Cox & Hawkesworth, 1985). Our trace element data confirm a sudden geochemical shift at this height, but a similar break in major elements and some radiogenic isotope ratios does not occur until another ~31 m higher (at ~965 m) in stratigraphy (Figures 4–6). These characteristics possibly indicate a gradual geochemical transition between the Ambenali and Mahabaleshwar formations rather than a sharp break due to a long volcanic hiatus of the order of 10^5 years.

5.2. Geochemical and Petrographic Indications for Four Eruption Sequences

The volcanic rocks sampled from the MP section display systematic geochemical variations with time, which cross the previously defined formation boundaries (Figures 4–6). Between the base of the profile and 200 m height, the eight flows show increasing TiO_2, FeO^T, Nb/Th, Ce/Pb, and La/Sm but decreasing MgO (Figures 4 and 5) (S1). A similar but more extensive trend (14 flows) is observed in the upper Poladpur lava into the Ambenali formation to a height of ~680 m with TiO_2 increasing from ~2 to ~3 wt.%, FeO^T increases from ~12 to ~17 wt.%, Nb/Th increasing from ~4 to ~10 and Ce/Pb increasing from ~10 to ~20 (Figures 4 and 5) (S2). A third sequence with eight flows begins at about 700 m height in the Ambenali formation and continues to 970 m height (Figures 4 and 5) (S3). A fourth sequence of 10 flows begins at 980 m height and is not clear in major element compositions but shows increasing Ce/Pb and Nb/Th as well as decreasing Nb/Zr to a height of 1,100 m (Figures 4 and 5) (S4).

Similar variations in major and trace element compositions have been observed in other LIPs (e.g., Moore et al., 2018, 2020; Yu et al., 2015) and geochemical modeling suggests that a combination of FC, recharge and eruption within RTF/REAFC-type magma reservoirs is required to explain such oscillatory signatures (K. G. Cox, 1988; Mittal et al., 2021; Yu et al., 2015). Detailed investigations on the influence of the melt influx, the eruption rate and the crystallization rate indicate first that all of these processes are essential and second that a continuous melt recharge of a few percentage of the reservoir mass is necessary (Mittal et al., 2021). Consistent with this, our new geochemical data suggest continuous melt recharge during the emplacement of each eruption sequence. For example, MgO correlates negatively with Nb/Th and Ce/Pb which indicate that the most primitive and hottest melts (highest MgO) were efficiently contaminated (lowest Nb/Th, Ce/Pb) (Figures 4, 5, and 7). However, the temporal increase in Nb/Th and Ce/Pb cannot be solely explained by less contamination but indicates continuous replenishment of the reservoir with less contaminated but more fractionated melt. In addition, the majority of lavas from the MP section exhibit glomeroporphyritic textures (Figure 3), which are believed to result from the mixing of successive recharge batches during the accumulation of magma reservoirs (e.g., Cashman et al., 2017; Krans et al., 2018; Moore et al., 2018). Accordingly, the recharge magmas derived

from melt accumulations deeper in the system transport mafic cumulates as crystal mush, which is flushed into magma reservoirs located in middle to upper crustal levels (e.g., Cashman et al., 2017; Krans et al., 2018). These multiple stages of melt ponding, transport, mixing, and eruption are recorded in the compositional zoning of plagioclase (Figure 3) (e.g., Borges et al., 2014). Most of the phenocrysts exhibit calcic interiors with high anorthite content (Figure 3), indicating the initial formation within a deep mafic magma reservoir. Rapid magmatic decompression due to fast melt ascent-caused resorption and the formation of sieve textures (Figure 3) (Nelson & Montana, 1992) until the melt was pooled into a magma reservoir at middle or upper crustal levels and underwent some FC. During the second stage of storage, the resorbed calcic interiors were overgrown by more sodic plagioclase, which could be related to the rapid drop in crystallization temperature (Barker et al., 1983; Cocker et al., 2021). Some phenocrysts exhibit multiple overgrowth rims, indicating several stages of melt ascent and storage during the emplacement of the MP lavas (Figure 3). The plagioclase phenocryst compositions and textures suggest relatively short residence times in smaller magma reservoirs located at different crustal levels. Within a long-lived large magma reservoir that receives continuous melt recharge, the residence times would be considerably longer, because the melts would be less likely to be erupted and the plagioclase phenocrysts would have developed oscillatory chemical zoning. Furthermore, a continuous recharge of a few percentage of the reservoir mass which is required to generate the oscillatory geochemical signatures is contrary to large magma reservoir models (Black & Manga, 2017; Mittal et al., 2021). For example, the influence of recharge-associated overpressure as main eruption trigger is inversely proportional to the total reservoir size implying that this process is unsuitable to cause eruptions of magma bodies with volumes between 10^5 and 10^6 km^3 comparable with the scale of the Wai Formations (e.g., Caricchi et al., 2014; Mittal et al., 2021).

We conclude that the geochemical variations in the MP lavas with time are best explained by a combination of magma mixing and recharge-associated overpressure leading to repeating melt recharge and FC sequences. The associated lavas were fed by multiple smaller magma reservoirs that were located in different crustal levels and interacted with each other as indicated by plagioclase phenocryst compositions and textures. The chemical trends thus reflect mixing between magmas stored at different depths in the crust undergoing variable crustal assimilation and FC. Quantitiave modeling of these processes is difficult, as many of the required variables (e.g., melt influx, eruption rates, reservoir sizes, contamination endmember compostions) are unknown. However, our new geochemcial data, together with published paleomagnetic data and absolute ages, provide a robust approach to draw conclusions about the magmatic processes that were associated with the emplacement of the MP lavas.

5.3. Indications for Continuous Volcanism During the Emplacement of the Wai Formations

The lavas of the Deccan CFB are separated by several red boles, indicating periods without volcanic activity. Based on U-Pb ages of zircons separated from these weathering horizons, it was previously argued that the lower seven Deccan Formations, the Poladpur Formation, the Ambenali Formation and the Mahabaleshwar Formation were erupted each in discrete pulses separated by volcanic hiatuses in the order of 10^4–10^5 years (Schoene et al., 2019). However, the S1 and S2, each of which indicates almost continuous FC and melt replenishment, span the Bushe-Poladpur and Poladpur-Ambenali boundary, respectively. The U-Pb age of the youngest red bole within the Bushe Formation (RBBI: 66.058 ± 0.039) is within the error of the U-Pb age of the oldest red bole within the Poladpur formation (RBBM: 66.06 ± 0.15 Ma) (Schoene et al., 2019), which is why the boundary between both formations could also be located lower in the stratigraphy (below the bottom of S1). However, based on geochemical characteristics, the lowermost sample from the MP profile can be clearly assigned to the Bushe Formation, while the overlying lava flow belongs to the Poladpur Formation, which could indicate continuous volcanic activity across the Bushe-Poladpur boundary. In comparison, the U-Pb age of the youngest red bole within the Poladpur Formation (RBX: 66.027 ± 0.062) is not within the error of the U-Pb ages of the oldest red bole within the Ambenali formation (RBBH: 65.885 ± 0.043) (Schoene et al., 2019), which could indicate a long break in volcanism between both formations (Schoene et al., 2019). In contrast, the MP lava belonging to S2 may reflect continuous FC and melt replenishment from the upper third of the Poladpur Formation to the middle of the Ambenali Formation which would argue against a volcanic hiatus in the order of 10^5 years and support the assumption that the Wai Formations (at least the Poladpur and Ambenali Formations) erupted continuously (Sprain et al., 2019) rather than in three discrete pulses (Schoene et al., 2019). Consistent with this, recent box models show that oscillatory geochemical signatures such as those observed for the lavas of the MP profile require almost constant melt recharge, implying continuous volcanism (Mittal et al., 2021). However, the lowermost part of the Ambenali Formation within the MP section is poorly sampled due to low-quality exposure. For

this reason, conclusions about volcanic activity across this boundary are limited and further sampling as well as geochemical analyzes are necessary.

5.4. Constraints on the Timescales of Magma Evolution and Eruption

The rocks used in this study were previously analyzed for paleomagnetic directions by Chenet et al. (2008), who proposed that adjacent lava flows that statistically have the same paleomagnetic directions (range of 5°–10°, so-called Directional Groups [DGs]) were formed within very short periods of time ($\sim 4 \times 10^2$ years) (Chenet et al., 2008). Rapid melt ascent during the eruption of the MP lava is supported by textural evidence observed in phenocrysts of plagioclase, which indicates fast magmatic decompression (Nelson & Montana, 1992). However, the quasi-cyclic nature of paleo-secular variation exhibits timescales in the order of 10^4 years that could cause spurious correlations wherein lava flows separated by multiple secular variation cycles still have a small difference in paleomagnetic directions (Mittal et al., 2021). Furthermore, many of the lavas of the MP section are separated from each other by red boles (Figures 4–6), indicating periods of volcanic quietness on the order of 10^1 to 5×10^4 years (Chenet et al., 2008; Duraiswami et al., 2020). Some of these red boles extend between samples of the same DG (Figures 4–6), which is inconsistent with a rapid eruption of the associated lava flows. However, due to the large uncertainty of time which is necessary for the formation of red boles, we assume that the DGs are reliable and can be used to estimate the timescales of magma evolution and eruption.

For the MP section, six DGs were defined with the total of all lava flows within DG is believed to erupted within $\sim 10^2$ years (Chenet et al., 2008). The DGs are located either at the bottom or top of a sequence (Figures 4–6). DG 1 is located at the top of S1, DG2 is located at the base of S2, DG3 and DG 4 are located at the base and top respectively of S3, and DG5 and DG 6 are located at the bottom and top respectively of S4 (Figures 4–6). These observations indicate that at the beginning and the end of each sequence, the associated melts erupt very fast. Rapid eruption at the beginning of a sequence could be due to the mixing of two magmas with different temperatures and compositions (early, relatively hot lavas with high MgO), which would cause recharge-associated overpressure. In contrast, the relatively fast eruptions at the end of a sequence are more likely due to buoyancy overpressure, which is caused by successive FC as indicated by decreasing MgO, Al_2O_3 and increasing TiO_2 and FeO^T (Figure 4) leading to volatile exsolution.

The lavas of the MP Profile are separated by several red boles indicating periods without volcanic activity (Figures 4–6). Zircons obtained from five of these weathering horizons were age dated (Schoene et al., 2019) yielding timestamps between individual eruptions (Figures 4–6). Between ~370 and ~700 m stratigraphic height, the upper half of the S2 is framed by two age-dated red boles providing temporal information about the associated processes and the lifespans of individual magma reservoirs (Figures 4–6). The time interval between both weathering horizons are $\sim 1.2 \times 10^5$ years, and the maximum and minimum values considering the measuring errors are 2.3×10^5 and 6×10^3 years, respectively. Between ~700 and ~1,000 m stratigraphic heights, the complete S3 and the lower part of S4 are framed by two age dated red boles (Figures 4–6). The time interval between both weathering horizons is $\sim 3.7 \times 10^5$ years, whereby the maximum and minimum values considering the measuring errors are 5.4×10^5 and 2.2×10^5 years, respectively. Although the age-dated horizons do not exactly bound individual sequences, it is evident that the latter erupted in time periods between $\sim 10^4$ and $\sim 10^5$ years.

Consistent with this, detailed studies comparing radiometric ages with intracrystalline diffusion durations of several lava flows show that individual magma reservoirs can be active for $\sim 10^5$ years (e.g., Cooper, 2019; Cooper & Kent, 2014). However, these long lifespans are only valid for upper-crustal and felsic magmatic systems (e.g., Cooper, 2019; Mutch et al., 2019) in contrast to the tholeiitic basaltic composition of the Poladpur to Mahabaleshwar lavas. In addition, there is no geophysical evidence for large continuous upper crustal intrusive bodies below India, which could represent former magma reservoirs with corresponding dimensions (Mittal et al., 2021; Prasad et al., 2018). The detected intrusions are prismatic in shape and have a diameter between 5 and 15 km as well as a thickness of few km (e.g., Prasad et al., 2018), which is contrary to a single large upper crustal magma reservoir with volumes between 10^5 and 10^6 km^3 (Mittal & Richards, 2021; Mittal et al., 2021). Thus, it is more likely that the lava within a sequence are associated with multiple smaller magma reservoirs, possibly with lifespans between 10^3 and 10^4 years (e.g., Mutch et al., 2019).

5.5. Rapid Shift in Composition and Depth of Contamination Endmembers

The lavas of the MP Profile show no continuous geochemical evolution with stratigraphic height (Figure 7). Instead, the MgO contents of the Bushe to Poladpur lavas (7.3–5.4 wt.%) overlap with those of the Ambenali

(6.8–5.2 wt.%) and Mahabaleshwar Formations (7.1–4.5 wt.%) indicating different mixing-fractional crystallization-eruption trends consistent with multiple magma reservoirs interacting with each other (Figures 7a and 7b). Between ~22 and ~934 m stratigraphic height, the ratios of source-sensitive trace elements and radiogenic isotopes gradually increased (Nb/Zr, εNd_{66Ma}) or decreased ($^{87}Sr/^{86}Sr_{66Ma}$, $^{206}Pb/^{204}Pb_{66Ma}$, $^{208}Pb/^{204}Pb_{66Ma}$) (Figures 5 and 6). These geochemical signatures could indicate that the magma reservoirs feeding the upper Bushe, Poladpur and Ambenali Formations exhibit a mantle source, that became progressively enriched and/or that the associated melts were successively less contaminated by continental crustal material. It was previously shown that the Ambenali lavas are the least contaminated Deccan lava and possibly represent a mixture of depleted Indian MORB and enriched Réunion hot spot mantle, whereby the portion of the latter successively increases over time (P. Lightfoot & Hawkesworth, 1988; Mahoney, 1988) (Figure 8). In comparison, the Poladpur and Bushe lavas are believed to represent a contamination of Ambenali-like magma with an Archean granitic crustal endmember that exhibits low values of εNd_{66Ma} (Figure 8) but high values of $^{206}Pb/^{204}Pb_{66Ma}$ and $^{87}Sr/^{86}Sr_{66Ma}$ (K. G. Cox & Hawkesworth, 1985; P. Lightfoot & Hawkesworth, 1988). Our new geochemical data show that the lavas of the Bushe and Poladpur Formations overlap with both lower and upper crustal components (Figure 8), which indicate several periods of storage and assimilation at different crustal levels, as also observed by multiple overgrowth rims in plagioclase phenocrysts (Figure 3).

There is no geochemical evidence for systematically increasing assimilation combined with FC (AFC) processes (e.g., Mahoney et al., 2000) (Figures 7c and 7d). If AFC processes had been important during the genesis of the Bushe, Poladpur and Ambenali lavas, the lava should exhibit positive correlations between MgO, Nb/Th, and Ce/Pb, indicating increasing contamination with increasing FC (Figures 7c and 7d). In contrast, the most primitive melts (with highest MgO contents) are the most contaminated (lowest Nb/Th and Ce/Pb), whereas more evolved melts display less contamination (e.g., K. Cox & Hawkesworth, 1984; K. G. Cox & Hawkesworth, 1985) (Figures 5, 6, 7c, and 7d). If each sequence were associated with processes within a single large magma reservoir, then the most primitive and hottest melt efficiently would have interacted with the wall rocks leading to high degrees of crustal contamination. In comparison, subsequent melts would be less contaminated since the most fusible parts were previously exhausted and cooling as well as FC during storage led to decreasing temperature and increasing number of mafic cumulates, which both had reduced the efficiency of crustal assimilation (Mittal & Richards, 2021; Yu et al., 2015). Although these processes would account for the overall decrease in contamination, they cannot explain the increase in Nb/Th and Ce/Pb in the melts with time. The increase in Nb/Th and Ce/Pb indicates continuous replenishment of the reservoir with less contaminated but more fractionated melt. Additionally, within a single large reservoir continuous recharge and tapping events would cause increasing MgO and oscillatory geochemical zoning in plagioclase contrary to the geochemical signatures and compositional normal zoning observed. Alternatively, the gradual increase in Nb/Th and Ce/Pb could reflect storage in multiple and small crustal magma reservoirs where they underwent variable extents of FC and assimilation. Within these reservoirs, crustal contamination is nearly absent, because previous melts exhausted the most fusible parts and their mafic cumulates formed a compositionally boundary layer that prevented the interaction with the wall rocks (Mittal & Richards, 2021). From these reservoirs, melts periodically erupt to the surface. The most primitive and hottest melts were contaminated in the lower crust where the country rocks are hotter (Annen et al., 2006), and possibly during turbulent ascent through the continental crust (e.g., Huppert et al., 1985). More evolved melts in the cooler upper crust assimilate less country rocks (Annen et al., 2006) and possibly follow the same ascent pathways as previous magmas, causing less contamination. The replenishment of the shallow magma reservoirs by hotter and more mafic magmas from the lower part of the magma plumbing system caused mixing and eruption. The trends of the four sequences imply that within each sequence, the magmas of the shallow, less contaminated reservoirs became more dominant, possibly reflecting less magma replenishment.

With the transition to the Mahabaleshwar Formation at ~934 m stratigraphic height, the ratios of La/Sm and Nb/Zr show a prominent shift toward higher values, which then gradually decrease again with time (Figure 5). In comparison, the ratios of Nb/Th and Ce/Pb as well as most major elements and radiogenic isotopes do not show similar geochemical changes until ~965 m stratigraphic height (Figures 4–6). The compositional change could indicate a change in the mantle source, but this would also cause variations in Nb/Zr and radiogenic Sr-Nd-Pb isotopes, which are not observed. If a change in the mantle source would be realistic, then the ratios of Nb/Zr as well as those of the radiogenic isotopes would remain high instead of decreasing with increasing stratigraphic height (Figures 5 and 6). Thus, it is unlikely that the shift to high La/Sm and Nb/Zr is due to a change of the mantle source of the magmas (Figures 5 and 6). Alternatively, these geochemical variations can be explained by

both variable degrees of melting and changing contamination endmembers. The Mahabaleshwar lavas exhibit low εNd_{66Ma}, $^{206}Pb/^{204}Pb_{66Ma}$, and $^{208}Pb/^{204}Pb_{66Ma}$ as well as moderate $^{87}Sr/^{86}Sr_{66Ma}$ different compared to upper crustal components (Figure 8). It was previously argued that the Mahabaleshwar Formation could be contaminated by the lithospheric mantle (P. Lightfoot & Hawkesworth, 1988; P. C. Lightfoot et al., 1990; Mahoney, 1988) or by amphibolites and mafic granulites that compose the lower continental crust (LCC) (e.g., Devey & Lightfoot, 1986). The contamination with lower crustal components is supported by radiogenic isotopes, but the Mahabaleshwar lava point toward much higher Nb/Zr. The Mahabaleshwar lavas display a negative correlation between La/Nb and La/Ba (Figure S1 in Supporting Information S1), which could indicate a strong lithospheric contribution (e.g., Jourdan et al., 2009). However, the negative trend between La/Nb and La/Ba does not correlate with Nb/Zr (Figure S1 in Supporting Information S1), which is why the lithospheric mantle cannot be considered as the sole contamination endmember. Based on geochemical characteristics, it cannot be clearly distinguished whether the Mahabaleshwar lavas were contaminated with the LCC and/or the lithospheric mantle. However, the circumstance that the contamination endmember shifted rapidly and not gradually from the upper crust to the lower crust or to the Moho or to the lithospheric mantle suggests that the MP lavas were fed by multiple magma reservoirs located in different crustal levels rather than by individual large ones.

5.6. Implications for the Architecture of the Magmatic Plumbing System

Modeling carried out in previous studies shows that oscillating geochemical signatures as observed for the lavas of the MP profile can be best explained by a combination of melt replenishment, fractional crystallization and eruption (K. G. Cox, 1988; Mittal et al., 2021; Yu et al., 2015). Thereby, it is necessary that the melted recharge is continuous and accounts for a few percentage of the total volume of the reservoir (Mittal et al., 2021). Furthermore, eruptions are predominantly triggered by recharge-associated overpressure which is inversely proportional to the reservoir volume (e.g., Caricchi et al., 2014; Mittal et al., 2021). These parameters indicate that the magmatic plumbing system that fed the MP lava was more likely to have consisted of several smaller magma reservoirs rather than a few large ones (Figure 9a). This is supported by the fact that geophysical studies do not find evidence for large, connected, upper crustal intrusive complexes, which could indicate magma reservoirs with corresponding dimensions beneath India (Patro & Sarma, 2016; Prasad et al., 2018). The detected intrusions are prismatic in shape and have diameters between ~5 and ~15 km as well as thicknesses of few km (Patro & Sarma, 2016; Prasad et al., 2018), which is contrary to a single large upper crustal magma reservoir with volumes between $\sim 10^5$ and $\sim 10^6$ km^3 (Mittal & Richards, 2021; Mittal et al., 2021). Although wide-angle seismic refraction surveys revealed that the Deccan Traps are underlain by high-velocity zones located at Moho depth possibly indicating thick ultramafic and mafic cumulate layers of lateral extensive magma reservoirs (Ridley & Richards, 2010), field observations from an exhumed lower crustal intrusive complex in Norway, which is believed to represent remnants of a deep LIP magmatic plumbing system, suggest that such structures do not necessarily represent individual magma bodies of equivalent size (Larsen et al., 2018; Mittal et al., 2021). This so-called Seiland Igneous Province consists of multiple ultramafic and mafic plutons separated from each other by chilled margins, indicating sequential emplacement of multiple small to medium-sized magma reservoirs (Larsen et al., 2018).

The lavas of the MP profile exhibit geochemical signatures indicating the assimilation of lower and upper crustal components (Figure 8). Consequently, the associated magma reservoirs were located at different crustal levels and interacted with each other, which is also supported by the mineral textures of plagioclase phenocrysts (Figures 3 and 9). Accordingly, primitive melts were contaminated with material of the LCC (amphibolite and granulite) and already underwent initial FC during which Ca-rich plagioclase crystals were formed (Figure 9b). Progressive FC in lower crustal reservoirs possibly led to volatile exsolution, which could have triggered buoyancy overpressure and rapid melt ascent during which plagioclase crystals were resorbed and sieve textures formed (Figure 9c). Mixing of the hot, mafic magmas with more evolved but less contaminated melts stored in the mid to upper crustal reservoirs triggered recharge-associated overpressure, which caused rapid eruption of less evolved (high MgO) but highly contaminated (low Nb/Th and Ce/Pb) lava flows at the beginning of each sequence (S1 to S4), as indicated by paleomagnetic directions and geochemical signatures. Before mixing, the shallow more evolved melts were less contaminated, because they were cooler, reacted with cooler wall rocks, and because the wall rocks may have been depleted in the most fusible portions due to reaction with earlier ascending magmas (Figure 9d). Further, due to storage and FC of previous melts, an increasing number of mafic cumulates could have formed a compositionally boundary layer which reduced or prevented crustal assimilation for subsequent

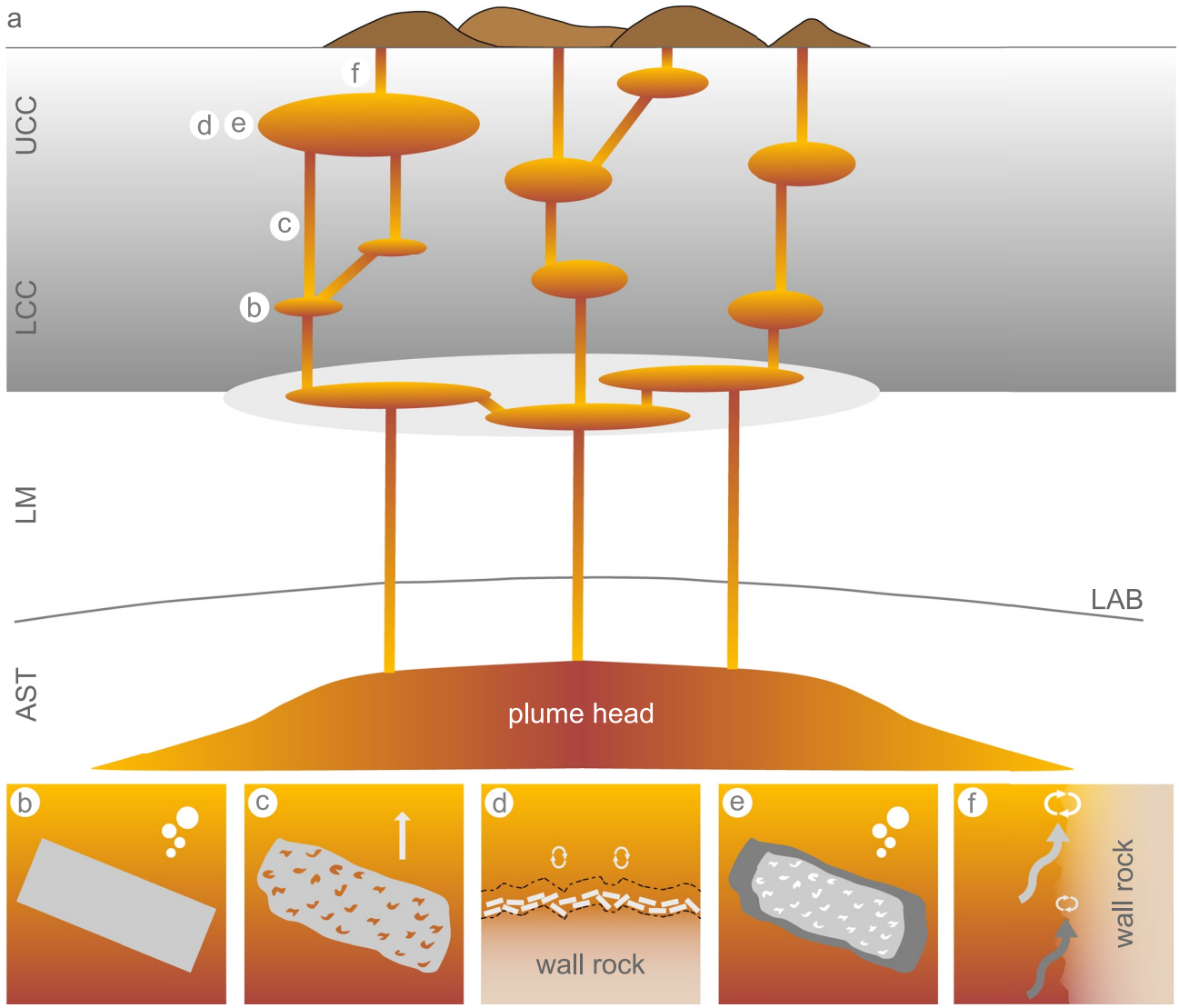

Figure 9. (a) Schematic sketch showing that the lavas of the MP profile were fed by multiple interconnected small- to medium-sized magma reservoirs located at different crustal levels. Figure modified after Mittal and Richards (2021) (b) Early fractional crystallization (FC) within deep magma reservoirs caused the formation of Ca-rich plagioclase crystals (gray rectangle) and volatile exsolution (white bubbles). (c) Rapid melt ascent (indicated by white arrow) caused resorption the of previously formed plagioclase and formation of sieve textures. (d) During storage in the mid to upper crustal magma reservoirs, the interaction with the wall rocks was prevented because the most fusible parts were previously exhausted (relative loss shown by dashed line) and mafic cumulates formed a compositional boundary plating layer which reduced the efficiency of crustal assimilation (indicated by small curved white arrows). (e) FC caused overgrown of resorbed ca-rich plagioclase crystals (light gray) by more sodic plagioclase (dark gray). White bubbles indicate volatile exsolution during progressive FC. (f) The melts erupted periodically and assimilated crustal material during turbulent ascent (indicated by waved arrows), with the most primitive and hottest melts (light gray waved arrow) were contaminated most efficiently (white curved arrow). Subsequent cooler and more differentiated melt (dark gray waved arrow), which preferentially followed the same pathways, were successively less contaminated due to continuous exhausting of the wall rocks (indicated by decreased size of curved white arrows). Abbreviations are as follows: UCC: upper continental crust; LCC: lower continental crust; LM: lithosphere mantle; AST: asthenosphere; and LAB: lithosphere-asthenosphere-boundary.

melts within the reservoirs (Figure 9d). After mixing and eruption, the mid to upper crustal reservoirs were continuously replenished by more evolved but less contaminated melts, resulting in periodic eruptions characterized by temporally decreasing MgO and increasing Nb/Th and Ce/Pb. During this stage, the resorbed phenocrysts were overgrown by more sodic plagioclase possibly due to a rapid drop in crystallization temperature (Figure 9e). Alternative or additional, the melts assimilated crustal material during turbulent ascent through the uppermost crust, with the most primitive and hottest melts were contaminated most efficiently (highest MgO, lowest Nb/Th and Ce/Pb). Subsequent cooler and more differentiated melt (lower MgO), which preferentially followed the same pathways, were successively less contaminated due to continuous exhaustion of the wall rocks (higher Nb/Th and Ce/Pb) (Figure 9f).

6. Conclusions

We conclude that major and trace element compositions, Sr-Nd-Pb isotope data, phenocryst textures and published paleomagnetic directions of 43 lava flows covering the most voluminous stage of the Deccan LIP (Bushe to Mahabaleshwar Formations) are best explained by four magmatic sequences (S1 to S4), which are characterized by continuous recharge, mixing, and the eruption of variably evolved melts from different crustal levels. Published zircon U-Pb age data obtained from weathered flow tops located between individual eruptions indicate that each of these magmatic sequences lasted $\sim10^4$–$\sim10^5$ years during which major and trace element compositions change systematically, followed by an abrupt change in geochemistry at the start of a new sequence. The lava at the beginning of each sequence generally have the highest MgO contents, but are the most contaminated (lowest Ce/Pb and Nb/Th). Subsequently, the MgO contents progressively decrease while the ratios of Nb/Th and Ce/Pb increase, implying continuous replenishment of the reservoir with more evolved but less contaminated melts. These geochemical signatures are supported by compositional zoning and sieve textures observed in plagioclase phenocrysts, indicating a complex interaction between multiple smaller magma reservoirs located at different crustal levels. Our new findings contribute to a better understanding of the establishement and temporal evolution of the magmatic plumbing system during the most voluminous stage of the Deccan LIP. The combination of geochemical and paleomagnetic data may also contribute to the general understanding of the architecture as well as the melt eruption rates during the main stages of other LIPs.

Data Availability Statement

All data produced during this study are provided in Tables S1 in Supporting Information S1 and Table S2 and are openly available in the EarthChem database at https://doi.org/10.26022/IEDA/112672.

Acknowledgments
We thank M. Hertel for helping with the XRF analyzes and C. Sporer for assistance in the initial sample processing. Further, we would like to thank M. Keith for helping with the electron microprobe analyzis. This work was funded by the Deutsche Forschungsgemeinschaft (DFG) (Grant HA2568/37-1). Open Access funding enabled and organized by Projekt DEAL.

References

Albarede, F., Luais, B., Fitton, G., Semet, M., Kaminski, E., Upton, B. G. J., et al. (1997). The geochemical regimes of Piton de la Fournaise volcano (Reunion) during the last 530 000 years. *Journal of Petrology*, *38*(2), 171–201. https://doi.org/10.1093/petroj/38.2.171

Alvarez, L. W., Alvarez, W., Asaro, F., & Michel, H. V. (1980). Extraterrestrial cause for the cretaceous-tertiary extinction. *Science*, *208*(4448), 1095–1108. https://doi.org/10.1126/science.208.4448.1095

Annen, C., Blundy, J. D., & Sparks, R. S. J. (2006). The Genesis of intermediate and silicic magmas in deep crustal hot zones. *Journal of Petrology*, *47*(3), 505–539. https://doi.org/10.1093/petrology/egi084

Barker, S. E., Kudo, A. M., & Keil, K. (1983). Mineral chemistry of basalts from holes 483 and 483B. In *Initial reports of the deep sea drilling project* (Vol. 65). U.S. Government Printing Office. https://doi.org/10.2973/dsdp.proc.65.130.1983

Basu, A. R., Renne, P. R., DasGupta, D. K., Teichmann, F., & Poreda, R. J. (1993). Early and late alkali igneous pulses and a high-^{3}He plume origin for the Deccan flood basalts. *Science*, *261*(5123), 902–906. https://doi.org/10.1126/science.261.5123.902

Basu, A. R., Saha-Yannopoulos, A., & Chakrabarty, P. (2020). A precise geochemical volcano-stratigraphy of the Deccan traps. *Lithos*, *376–377*, 105754. https://doi.org/10.1016/j.lithos.2020.105754

Beane, J. E., Turner, C. A., Hooper, P. R., Subbarao, K. V., & Walsh, J. N. (1986). Stratigraphy, composition and form of the Deccan basalts, Western Ghats, India. *Bulletin of Volcanology*, *48*(1), 61–83. https://doi.org/10.1007/BF01073513

Black, B. A., & Manga, M. (2017). Volatiles and the tempo of flood basalt magmatism. *Earth and Planetary Science Letters*, *458*, 130–140. https://doi.org/10.1016/j.epsl.2016

Borges, M. R., Sen, G., Hart, G. L., Wolff, J. A., & Chandrasekharam, D. (2014). Plagioclase as recorder of magma chamber processes in the Deccan traps: Sr-Isotope zoning and implications for Deccan eruptive event. *Journal of Asian Earth Sciences*, *84*, 95–101. https://doi.org/10.1016/j.jseaes.2013.10.034

Bosch, D., Blichert-Toft, J., Moynier, F., Nelson, B. K., Telouk, P., Gillot, P.-Y., & Albarède, F. (2008). Pb, Hf and Nd isotope compositions of the two réunion volcanoes (Indian Ocean): A tale of two small-scale mantle "blobs". *Earth and Planetary Science Letters*, *265*(3–4), 748–765. https://doi.org/10.1016/j.epsl.2007.11.018

Bryan, S. E., & Ernst, R. E. (2008). Revised definition of large igneous provinces (LIPs). *Earth-Science Reviews*, *86*(1–4), 175–202. https://doi.org/10.1016/j.earscirev.2007.08.008

Caricchi, L., Annen, C., Blundy, J., Simpson, G., & Pinel, V. (2014). Frequency and magnitude of volcanic eruptions controlled by magma injection and buoyancy. *Nature Geoscience*, *7*(2), 126–130. https://doi.org/10.1038/ngeo2041

Cashman, K. V., Sparks, R. S. J., & Blundy, J. D. (2017). Vertically extensive and unstable magmatic systems: A unified view of igneous processes. *Science*, *355*(6331), 355. https://doi.org/10.1126/science.aag3055

Chauvel, C., & Blichert-Toft, J. (2001). A hafnium isotope and trace element perspective on melting of the depleted mantle. *Earth and Planetary Science Letters*, *190*(3–4), 137–151. https://doi.org/10.1016/S0012-821X(01)00379-X

Chenet, A.-L., Fluteau, F., Courtillot, V., Gérard, M., & Subbarao, K. V. (2008). Determination of rapid Deccan eruptions across the Cretaceous-Tertiary boundary using paleomagnetic secular variation: Results from a 1200-m-thick section in the Mahabaleshwar escarpment. *Journal of Geophysical Research*, *113*(B4), B04101. https://doi.org/10.1029/2006JB004635

Cocker, K., Shane, P., Stirling, C. H., & Reid, M. R. (2021). Constraints on assembly of Tongariro and Ruapehu andesite magmas based on Sr-isotope compositions of plagioclase and groundmass. *Lithos*, *400–401*, 106406. https://doi.org/10.1016/j.lithos.2021.106406

Cooper, K. M. (2019). Time scales and temperatures of crystal storage in magma reservoirs: Implications for magma reservoir dynamics. *Philosophical Transactions of the Royal Society A: Mathematical, Physical & Engineering Sciences*, *377*(2139), 20180009. https://doi.org/10.1098/rsta.2018.0009

Cooper, K. M., & Kent, A. J. R. (2014). Rapid remobilization of magmatic crystals kept in cold storage. *Nature*, *506*(7489), 480–483. https://doi.org/10.1038/nature12991

Courtillot, V., Besse, J., Vandamme, D., Montigny, R., Jaeger, J.-J., & Cappetta, H. (1986). Deccan flood basalts at the Cretaceous/Tertiary boundary? *Earth and Planetary Science Letters*, *80*(3–4), 361–374. https://doi.org/10.1016/0012-821X(86)90118-4

Cox, K. G. (1988). Numerical modelling of a randomized RTF magma chamber: A comparison with continental flood basalt sequences. *Journal of Petrology*, *29*(3), 681–697. https://doi.org/10.1093/petrology/29.3.681

Cox, K. G., & Hawkesworth, C. J. (1985). Geochemical stratigraphy of the Deccan traps at Mahabaleshwar, Western Ghats, India, with implications for open system magmatic processes. *Journal of Petrology*, *26*(2), 355–377. https://doi.org/10.1093/petrology/26.2.355

Cox, K., & Hawkesworth, C. (1984). Relative contribution of crust and mantle to flood basalt magmatism, Mahabaleshwar area, Deccan traps. *Philosophical Transactions of the Royal Society of London - Series A: Mathematical and Physical Sciences*, *310*, 627–641. https://doi.org/10.1098/rsta.1984.0011

Devey, C. W., & Lightfoot, P. C. (1986). Volcanological and tectonic control of stratigraphy and structure in the western Deccan traps. *Bulletin of Volcanology*, *48*(4), 195–207. https://doi.org/10.1007/BF01087674

Duraiswami, R. A., Sheth, H., Gadpallu, P., Youbi, N., & Chellai, E. H. (2020). A simple recipe for red bole formation in continental flood basalt provinces: Weathering of flow-top and flow-bottom breccias. *Arabian Journal of Geosciences*, *13*(18), 953. https://doi.org/10.1007/s12517-020-05973-9

Elkins-Tanton, L. T., & Foulger, G. R. (2005). Continental magmatism caused by lithospheric delamination. *Geological Society of America Special Paper*, *388*, 449–461. https://doi.org/10.1130/2005.2388(27)

Ernst, R. E., Buchan, K. L., & Campbell, I. H. (2005). Frontiers in large igneous province research. *Lithos*, *79*(3–4), 271–297. https://doi.org/10.1016/j.lithos.2004.09.004

Glišović, P., & Forte, A. M. (2017). On the deep-mantle origin of the Deccan traps. *Science*, *355*(6325), 613–616. https://doi.org/10.1126/science.aah4390

Hoyer, P. A., Haase, K. M., Regelous, M., O'Connor, J. M., Homrighausen, S., Geissler, W. H., & Jokat, W. (2022). Mantle plume and rift-related volcanism during the evolution of the Rio Grande Rise. *Communications Earth & Environment*, *3*(1), 18. https://doi.org/10.1038/s43247-022-00349-1

Hoyer, P. A., Regelous, M., Adatte, T., & Haase, K. M. (2022). Machine learning-based re-classification of the geochemical stratigraphy of the Rajahmundry Traps, India. *Journal of Volcanology and Geothermal Research*, *428*, 107594. https://doi.org/10.1016/j.jvolgeores.2022.107594

Huppert, H. E., Stephen, R., & Sparks, J. (1985). Cooling and contamination of mafic and ultramafic magmas during ascent through continental crust. *Earth and Planetary Science Letters*, *74*(4), 371–386. https://doi.org/10.1016/S0012-821X(85)80009-1

Jay, A. E. (2005). Volcanic architecture of the Deccan traps, western Maharashtra, India: An integrated chemostratigraphic and paleomagnetic study.

Jay, A. E., & Widdowson, M. (2008). Stratigraphy, structure and volcanology of the SE Deccan continental flood basalt province: Implications for eruptive extent and volumes. *Journal of the Geological Society*, *165*(1), 177–188. https://doi.org/10.1144/0016-76492006-062

Jourdan, F., Bertrand, H., Féraud, G., le Gall, B., & Watkeys, M. K. (2009). Lithospheric mantle evolution monitored by overlapping large igneous provinces: Case study in southern Africa. *Lithos*, *107*(3–4), 257–268. https://doi.org/10.1016/j.lithos.2008.10.011

Karlstrom, L., & Richards, M. (2011). On the evolution of large ultramafic magma chambers and timescales for flood basalt eruptions. *Journal of Geophysical Research*, *116*(B8), B08216. https://doi.org/10.1029/2010JB008159

Krans, S. R., Rooney, T. O., Kappelman, J., Yirgu, G., & Ayalew, D. (2018). From initiation to termination: A petrostratigraphic tour of the Ethiopian low-Ti flood basalt province. *Contributions to Mineralogy and Petrology*, *173*(5), 1–22. https://doi.org/10.1007/s00410-018-1460-7

Kumar, P., & Chaubey, A. K. (2022). Réunion plume associated flood basalt volcanism on the northwestern continental margin of India and related tectonics. *Journal of Asian Earth Sciences*, *237*, 105352. https://doi.org/10.1016/j.jseaes.2022.105352

Larsen, R. B., Grant, T., Sørensen, B. E., Tegner, C., McEnroe, S., Pastore, Z., et al. (2018). Portrait of a giant deep-seated magmatic conduit system: The Seiland Igneous Province. *Lithos*, *296–299*, 600–622. https://doi.org/10.1016/j.lithos.2017.11.013

Lightfoot, P. C., Hawkesworth, C. J., Devey, C. W., Rogers, N. W., & Calsteren, P. W. C. V. (1990). Source and differentiation of Deccan trap lavas: Implications of geochemical and mineral chemical variations. *Journal of Petrology*, *31*(5), 1165–1200. https://doi.org/10.1093/petrology/31.5.1165

Lightfoot, P., & Hawkesworth, C. (1988). Origin of Deccan trap lavas: Evidence from combined trace element and Sr-Nd- and Pb-isotope studies. *Earth and Planetary Science Letters*, *91*(1–2), 89–104. https://doi.org/10.1016/0012-821X(88)90153-7

Luais, B. (2004). Temporal changes in Nd isotopic composition of Piton de la Fournaise magmatism (Réunion Island, Indian Ocean). *Geochemistry, Geophysics, Geosystems*, *5*(1), Q01008. https://doi.org/10.1029/2002GC000502

Mahoney, J. J. (1988). Deccan traps. In *Continental flood basalts* (pp. 151–194). Springer.

Mahoney, J. J., Sheth, H. C., Chandrasekharam, D., & Peng, Z. X. (2000). Geochemistry of Flood Basalts of the Toranmal Section, Northern Deccan Traps, India: Implications for Regional Deccan Stratigraphy. *Journal of Petrology*, *41*(7), 1099–1120. https://doi.org/10.1093/petrology/41.7.1099

Mittal, T., & Richards, M. A. (2021). The magmatic architecture of continental flood basalts II: A new conceptual model. *Journal of Geophysical Research: Solid Earth*, *126*(12), e2021JB021807. https://doi.org/10.1029/2021JB021807

Mittal, T., Richards, M. A., & Fendley, I. M. (2021). The magmatic architecture of continental flood basalts I: Observations from the Deccan traps. *Journal of Geophysical Research: Solid Earth*, *126*(12), e2021JB021808. https://doi.org/10.1029/2021JB021808

Moore, N. E., Grunder, A. L., & Bohrson, W. A. (2018). The three-stage petrochemical evolution of the Steens Basalt (southeast Oregon, USA) compared to large igneous provinces and layered mafic intrusions. *Geosphere*, *14*(6), 2505–2532. https://doi.org/10.1130/ges01665.1

Moore, N. E., Grunder, A. L., Bohrson, W. A., Carlson, R. W., & Bindeman, I. N. (2020). Changing mantle sources and the effects of crustal passage on the Steens Basalt, SE Oregon: Chemical and isotopic constraints. *Geochemistry, Geophysics, Geosystems*, *21*(8), e2020GC008910. https://doi.org/10.1029/2020gc008910

Mutch, E. J. F., Maclennan, J., Holland, T. J. B., & Buisman, I. (2019). Millennial storage of near-Moho magma. *Science*, *365*(6450), 260–264. https://doi.org/10.1126/science.aax4092

Najafi, S. J., Cox, K. G., & Sukheswala, R. N. (1981). Geology and geochemistry of the basalt flows (Deccan Traps) of the Mahad-Mahableshwar section, India. *Memoir - Geological Society of India*, *3*, 300–315.

Nelson, S. T., & Montana, A. (1992). Sieve-textured plagioclase in volcanic rocks produced by rapid decompression. *American Mineralogist*, *77*, 1242–1249.

Patro, P. K., & Sarma, S. V. S. (2016). Evidence for an extensive intrusive component of the Deccan Large Igneous Province in the Narmada Son Lineament region, India from three dimensional magnetotelluric studies. *Earth and Planetary Science Letters*, *451*, 168–176. https://doi.org/10.1016/j.epsl.2016.07.005

Prasad, K. N. D., Singh, A. P., & Tiwari, V. M. (2018). 3D upper crustal density structure of the Deccan Syneclise, Central India. *Geophysical Prospecting*, *66*(8), 1625–1640. https://doi.org/10.1111/1365-2478.12675

Punekar, J., Mateo, P., & Keller, G. (2014). Effects of Deccan volcanism on paleoenvironment and planktic foraminifera: A global survey. *Geological Society of America Special Paper*, *505*, 91–116. https://doi.org/10.1130/2014.2505(04)

Richards, M. A., Alvarez, W., Self, S., Karlstrom, L., Renne, P. R., Manga, M., et al. (2015). Triggering of the largest Deccan eruptions by the Chicxulub impact. *The Geological Society of America Bulletin*, *127*(11–12), 1507–1520. https://doi.org/10.1130/B31167.1

Richards, M. A., Duncan, R. A., & Courtillot, V. E. (1989). Flood basalts and hot-spot tracks: Plume heads and tails. *Science*, *246*(4926), 103–107. https://doi.org/10.1126/science.246.4926.103

Ridley, V. A., & Richards, M. A. (2010). Deep crustal structure beneath large igneous provinces and the petrologic evolution of flood basalts. *Geochemistry, Geophysics, Geosystems*, *11*(9), Q09006. https://doi.org/10.1029/2009GC002935

Schoene, B., Eddy, M. P., Samperton, K. M., Keller, C. B., Keller, G., Adatte, T., & Khadri, S. F. R. (2019). U-Pb constraints on pulsed eruption of the Deccan traps across the end-Cretaceous mass extinction. *Science*, *363*(6429), 862–866. https://doi.org/10.1126/science.aau2422

Self, S., Mittal, T., Dole, G., & Vanderkluysen, L. (2022). Toward understanding Deccan volcanism. *Annual Review of Earth and Planetary Sciences*, *50*(1), 477–506. https://doi.org/10.1146/annurev-earth-012721-051416

Self, S., Schmidt, A., & Mather, T. A. (2014). Emplacement characteristics, time scales, and volcanic gas release rates of continental flood basalt eruptions on Earth. In *Volcanism, impacts, and mass extinctions: Causes and effects*. Geological Society of America. https://doi.org/10.1130/2014.2505(16

Sepkoski, J. J. (1996). Patterns of phanerozoic extinction: A perspective from global data bases. In *Global events and event stratigraphy in the phanerozoic* (pp. 35–51). Springer.

Sprain, C. J., Renne, P. R., Vanderkluysen, L., Pande, K., Self, S., & Mittal, T. (2019). The eruptive tempo of Deccan volcanism in relation to the Cretaceous-Paleogene boundary. *Science*, *363*(6429), 866–870. https://doi.org/10.1126/science.aav1446

Wang, A., Liu, Y., Santosh, M., & Gu, X. (2013). Zircon U-Pb geochronology, geochemistry and Sr-Nd-Pb isotopes from the metamorphic basement in the Wuhe Complex: Implications for Neoarchean active continental margin along the southeastern North China Craton and constraints on the petrogenesis of Mesozoic granitoids. *Geoscience Frontiers*, *4*(1), 57–71. https://doi.org/10.1016/j.gsf.2012.05.001

White, R., & McKenzie, D. (1989). Magmatism at rift zones: The generation of volcanic continental margins and flood basalts. *Journal of Geophysical Research*, *94*(B6), 7685–7729. https://doi.org/10.1029/JB094iB06p07685

Yu, X., Lee, C.-T. A., Chen, L.-H., & Zeng, G. (2015). Magmatic recharge in continental flood basalts: Insights from the Chifeng igneous province in Inner Mongolia. *Geochemistry, Geophysics, Geosystems*, *16*(7), 2082–2096. https://doi.org/10.1002/2015GC005805